Chapter 4. Results and Discussion

To facilitate the evaluation of the bone-specific ECM synthesis in the chitosan/gelatin/hydroxyapatiite scaffold materials, they were compared for their properties, both before and after being seeded with either rT or rM. The product parameters were set up to decide on to most suitable scaffolds which present features similar to natural bone for bone tissue engineering.

4.1 Scaffold Material Characterization

4.1.1 Macroscopic evaluation

The group of scaffolds developed through gelate-freeze-drying allowed direct shaping to match the bone defect geometry in terms of specific 3D shape. Naked eye-view of the synthesized scaffolds is indicated as in **Figure 4.1**.

4.1.2 Microscopic evaluation

4.1.2.1 Surface morphology

Atomic Force Microscopy (AFM) topographies were used to calculate surface roughness of the scaffold biomaterial and displayed in **Table 4.1**. It was seen that at the microscopic scale, the surface roughness affected the osteogenic cell's surface anchoring and attachment property.

The AFM data in **Figure 4.1** and **Table 4.1** depicted surface roughness, and observed to be the least in the scaffold composite without gelatin i.e. CH. Hence, gelatin inclusion leads to increase in surface roughness as observed for CG, GH and CGH.

Also observed from the previous studies [13,126], increased surface roughness

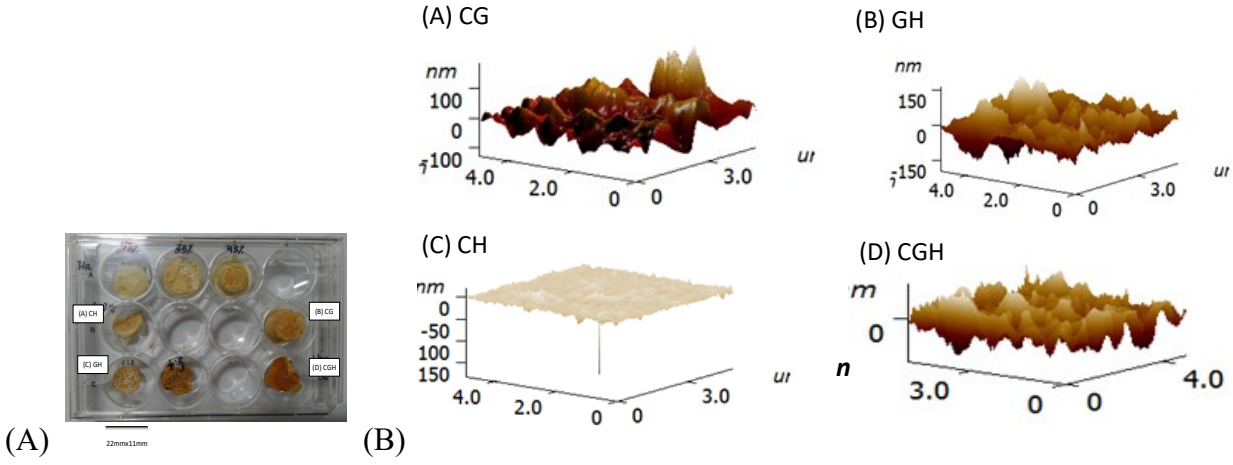

Figure 4.1 (A) Representative naked-eye-view of the scaffold material and (B) 3D AFM graph of the scaffolds: (A) CG, (B) GH, (C) CH and (D) CGH.

corresponded to favouable cell attachment and smooth surface corresponded to favourable cell proliferation.

Sample No.	Roughness average (nm)	Skewness	Kurtosis	Root mean square roughness
#1 CH	0.186 um	-0.469	3.948	0.249 um
#2 CG	5.081 nm	1.120	16.615	7.833 nm
#3 GH	42.908 nm	-1.052	16.882	103.448 nm
#4 CGH	14.963 nm	1.875	17.591	21.707 nm

Table 4.1 Surface roughness parameters shown as mean ±SD from the AFM image of the scaffolds (n=5).

As seen in **Table 4.1**, the surface roughness is following the decreasing order for the scaffold as: GH>CGH>CG>CH.

Hence, maximun proliferation potential could be attributed in the 'CH' scaffold material and maximum proliferation in 'GH'. This gives the impression that Ha have cell function supporting behavior in addition to the polymerization effect on the scaffold materials [5]. Also, with the increase in gelatin loading, surface roughness has increased for the scaffold. It leads to the formation of agglomerates on the scaffold materials predominantly on the surface when present in association with gelatin [199]. According to the obtained result, chitosan contributed in decreasing the surface roughness when present in combination with either gelatin or Ha. When alone, chitosan presents a

smoothen surface also presented by the previous studies [200]. Contrary to the result reported in [111] wherein Ha alone contributes to additional roughness has not been found in this study.

4.1.2.2 Core Morphology

The individual constituents used to fabricate the scaffolds were evaluated too. Firstly, the core morphology of the constituents was determined by SEM analysis and are displayed in **Figure 4.3.**

'Gelatin only' slurry when moulded formed heterogeneous porous architecture at micro-scale. The 'Ha only' structure displayed minisicule aggregates indicating multiple small aggregates as Ha crystallites themselves of ~50nm. From **Figure 4.3B**, Ha SEM showed white needle shaped crystals of average size of 50±0.5nm.

The pore wall appeared rough with reduced porosities. 'Chitosan only' structure showed the bestest homogeneous porous assembly with uniform particle size of ~200nm.

The pores were oval and well interconnected [201].

(A) Gelatin only

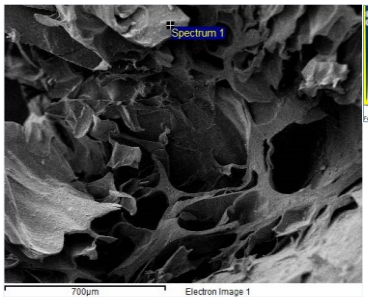

Element	Weight%	Atomic%
C K	43.88	54.32
O K	44.21	41.08
P K	1.67	0.80
Ca K	10.24	3.80
Totals	100.00	

(B) Hydroxyapatite only

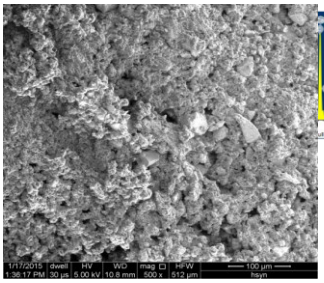

Element	Weight%	Atomic%
C K	72.30	75.96
O K	33.76	26.62
P K	1.24	0.39
Ca K	7.3	2.97
Totals	100.00	

(C) Chitosan only

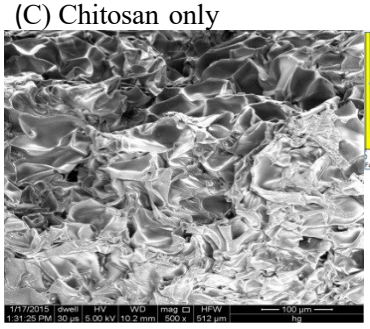

Element	Weight%	Atomic%
C K	67.22	73.20
O K	32.78	26.80
Totals	100.00	

(D) Crystal content

Sr. No.	Sample	Ca/P*
1.	Chitosan	Absent
2.	Gelatin	4.75
3.	Hydroxylapatite	5.88

Figure 4.3 SEM-EDX spectrum of the individual constituents present in the scaffold materials: (A-C) and the comparative display of crystal content in terms of Ca/P from EDX spectrum: (D).

Porous interconnected architecture observed from qualitative-SEM of the different scaffold biomaterials is shown in **Figure 4.4**.

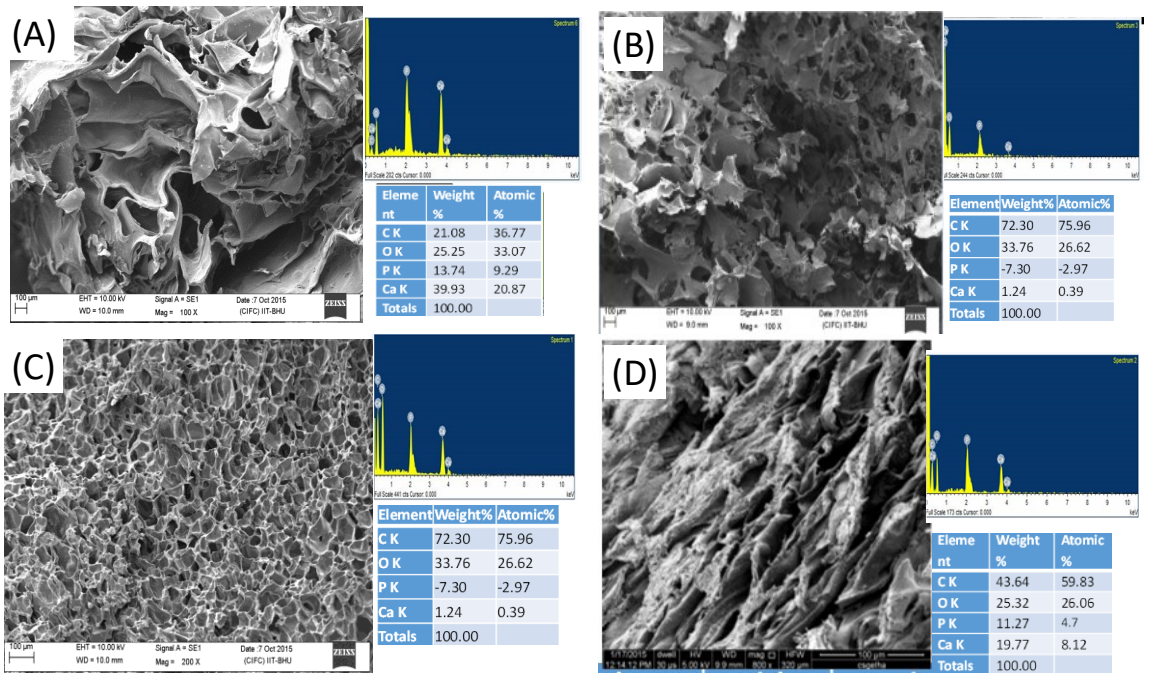

Figure 4.4 SEM-EDX spectrum of the scaffold materials: (A) CG, (B) CGH, (C) CH and (D) GH.

Every scaffold samples exhibited homogeneous morphology in terms of porous structure providing template for tissue growth. Gelatin matrix based biomaterial **(Figure 4.4 A, C & D**) display open pore structure in the form of ellipse whereas CH display uniform but less elongated shape also observed in previous work [202,203].

4.1.2.3 Elemental Mapping

The CaP content determined after the elemental mapping of the biomaterials is summarised in **Table 4.2**.

Sample No.	Ca/P
#1 CH	1.77
#2 CG	2.24
#3 GH	0.13

#4 CGH	1.72

Table 4.2 Scaffold Ca/P derived from the EDX spectrum analysis.

Among all the biomaterials GH presented highest Ca/P content. From the Ca/P of Ha [204], in CGH the Ca/P content observed closest to the natural bone. Hence, least CaP in CH indicate the role of gelatin in mineral deposition [58].

In all the four scaffolds, the chitosan, gelatin and Ha do not exist as separate entities and have been uniformly dispersed into a scaffold unit. From SEM image the measured pore size of CG, CH, GH and CGH scaffold was found to be 255±4.5µm, 150±7µm, 277±34µm and 200±91µm. It was observed that with the addition of chitosan decrease in the pore size was observed for GH and CH of scaffold and in CG the pore shape became irregular with the increase in pore volume. The variations in pore structures from circular, lamellar, elliptical and coral-reef were found from SEM images too.

4.1.2.4 TEM-SAED

From bright-field TEM-SAED in **Figure 4.5**, uniformity in structure is observed in all the biomaterial samples.

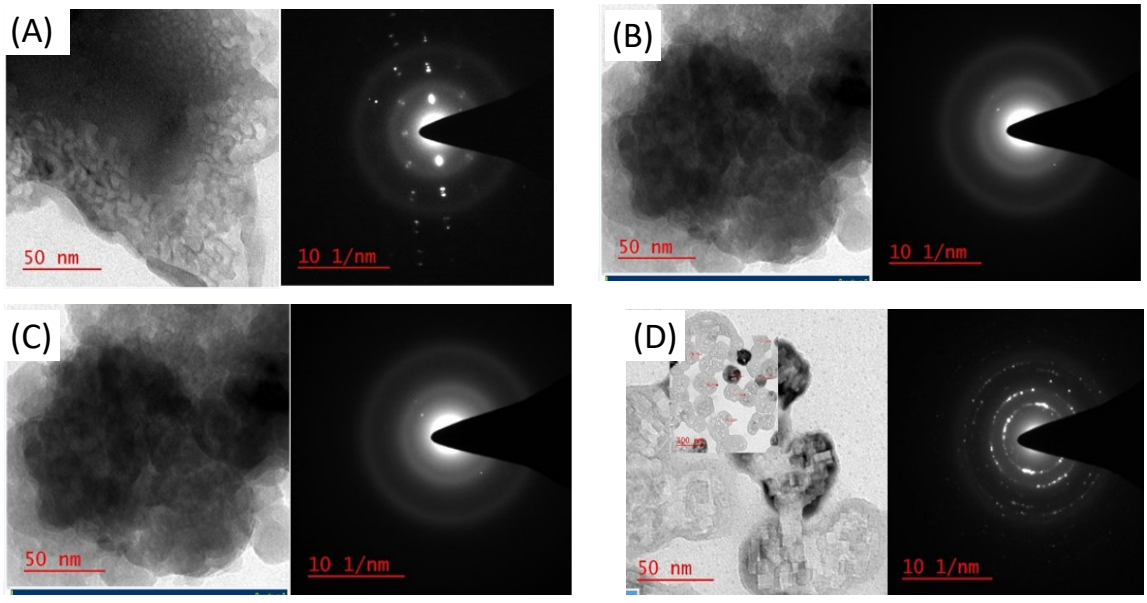

Figure 4.5. Morphological characteristics of composites sectioned as TEM image of pore structure and SAED displaying crystal spots and diffraction ring: A. CG, B. GH, C. CH and D. CGH.

The biomaterial scaffolds exhibited different morphology then their constituents. Both particle size and pore size controlled by the gelatin induced dispersion as depicted in TEM images of gelatin containing biomaterials (**Figure 4.5).** Similar observations have been reported by J.Ran [205]. The TEM images of CGH scaffolds displayed uniform porous architecture, with circular micropores observed as a grape-bunch.

From SAED, the crystalline nature of hydroxylapatite is more prominent in CH. The series of discrete strong spots with multiple crystal degree of order are visible in the **Figure 4.5.** The distinct crystal spots in the diffraction ring were very sharp in CGH scaffold samples. It indicated that the crystalline nature was prominent in CGH. From SAED, crystallinity of the scaffolds follows the order: CG<GH<CH<CGH. Diffused particles, two crystal spots and 2-5 crystal spots were visible in CG, GH and CH, respectively.

4.1.3 Physicochemical characterization

The composition of the mineral layer deposited after the cell-biomaterial interaction is depicted in the XRD and FTIR peaks.

4.1.3.1 XRD

The XRD of raw materials showed peak values at 25.8°, 31.7° and 48.5°, which mark the characteristic peaks of carbonated Ha [206]. The diffraction pattern of hydroxyapatute imply the presence of the major planes for (002),(211) and (300) at 25°, 31°, 32° 2θ angles as shown in **Figure 4.6** and absence of secondary phase, which established the purity of the prepared inorganic raw material. From **Figure 4.6** and **Table 4.3**, Ha peaks revealed it to be crystalline and no second phases were detected.

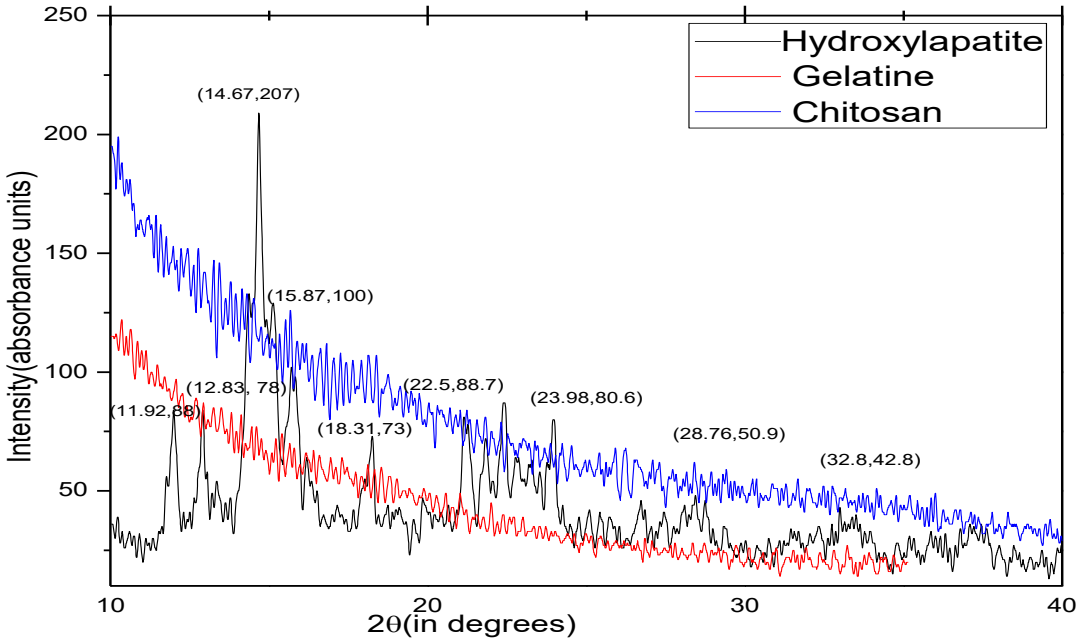

Figure 4.6 XRD spectra of the scaffold constituents i.e. Chitosan, Gelatin and Hydroxyapatite.

Sr.No.	Raw material	2θ (in degrees)
1.	Chitosan	10.5, 20.2
2.	Gelatin	20.25
3.	Ha	25.98,31.76, 32.8, 34, 49.56

Table 4.3 Characteristic XRD peaks of the scaffold constituents.

From XRD of the Scaffold Materials in **Figure 4.7**, the peak broadening in all the biomaterials indicate decrease in the crystalline nature of hydroxylapatite when it co-exists as biomaterial component. The crystal planes of hydroxylapatite are shown in detail in **Figure 4.7** exhibiting resemblance to the natural bone structure [138].

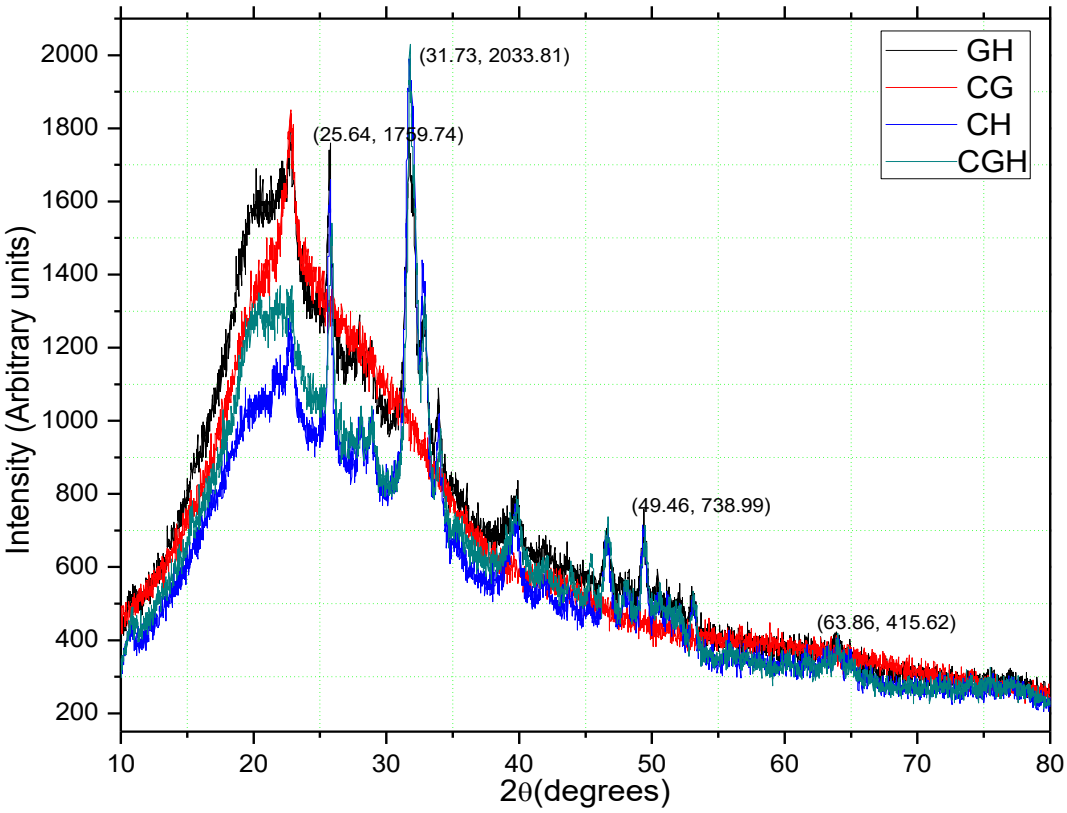

Figure 4.7 XRD Intensities (I, in arbitrary units, a.u.) of the scaffold materials.

The minimum reduction in crystalline behaviour observed in the CH labelled scaffold, thereby indicate the role of gelatin in reducing the Ha crystallinity in remaining scaffold groups (CG, GH and CGH). The characteristic peaks of chitosan (20.305°, 29.96°) were found in the CGH scaffold [207].

4.1.3.2 FTIR

The results from FTIR defining the chemical fingerprint of the biomaterial determines the identity, composition, and consistency of the biomaterial. In order to compare the chemical bonding within the biomaterial and in the constituent raw materials, the intensities of the characteristic chemical groups of all the three constituents are displayed in **Figure 4.8** and are summarised in **Table 4.4**.

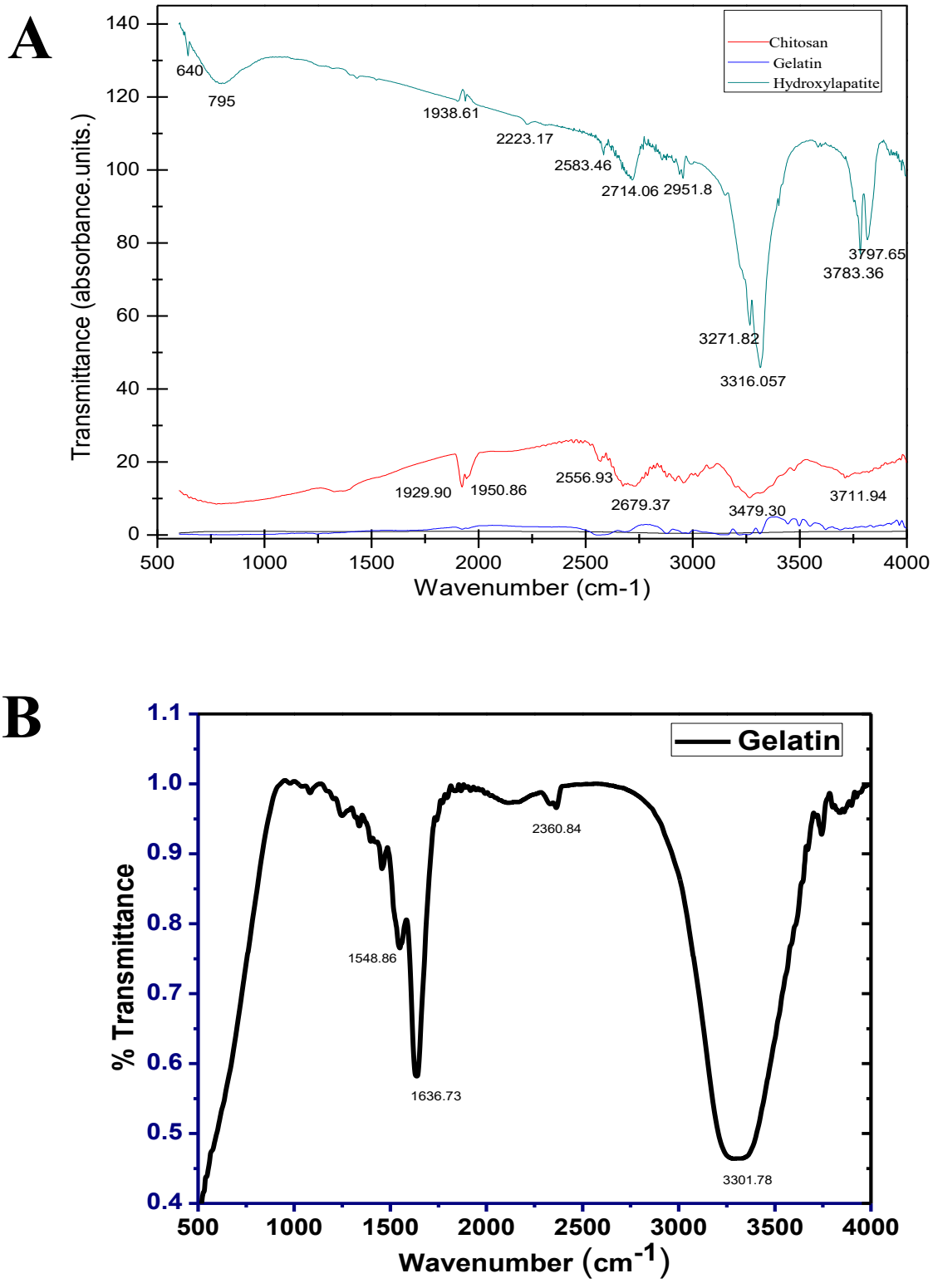

Figure 4.8 Display of the characteristic FTIR spectra of the scaffold constituents.

Raw material	Transmittance Intensity (±5cm^{-1})	Characteristic Linkages
Chitosan	898	C–N band [72]
	1150 to 1000	'combination vibration' bands with the sugar rings
	1154 to 1032	C–O–C linkage
	1423 and 1380	CH_2 and CH_3 vibrations
	1650 and 1560	Scanty amount of C–NH_2
	2920 and 2881	CH stretching vibration
	3420	stretching vibrations from NH_2 and OH
Gelatin	1077	C–O–C stretching mode
	1539	NH bending
	1648	C=O stretching
	2930	C-H stretching
	3444	N/H stretching of 2° amide
	900-1400	PO_4 vibration
Ha	470, 560, 600, 952,	Phosphate group
	1030	
	1405	$C00_3^-$
	1640	Bending mode of OH
	3435	Water molecule & OH stretching vibration

Table 4.4 Characteristic groups displaying transmittance intensities of the scaffold constituents.

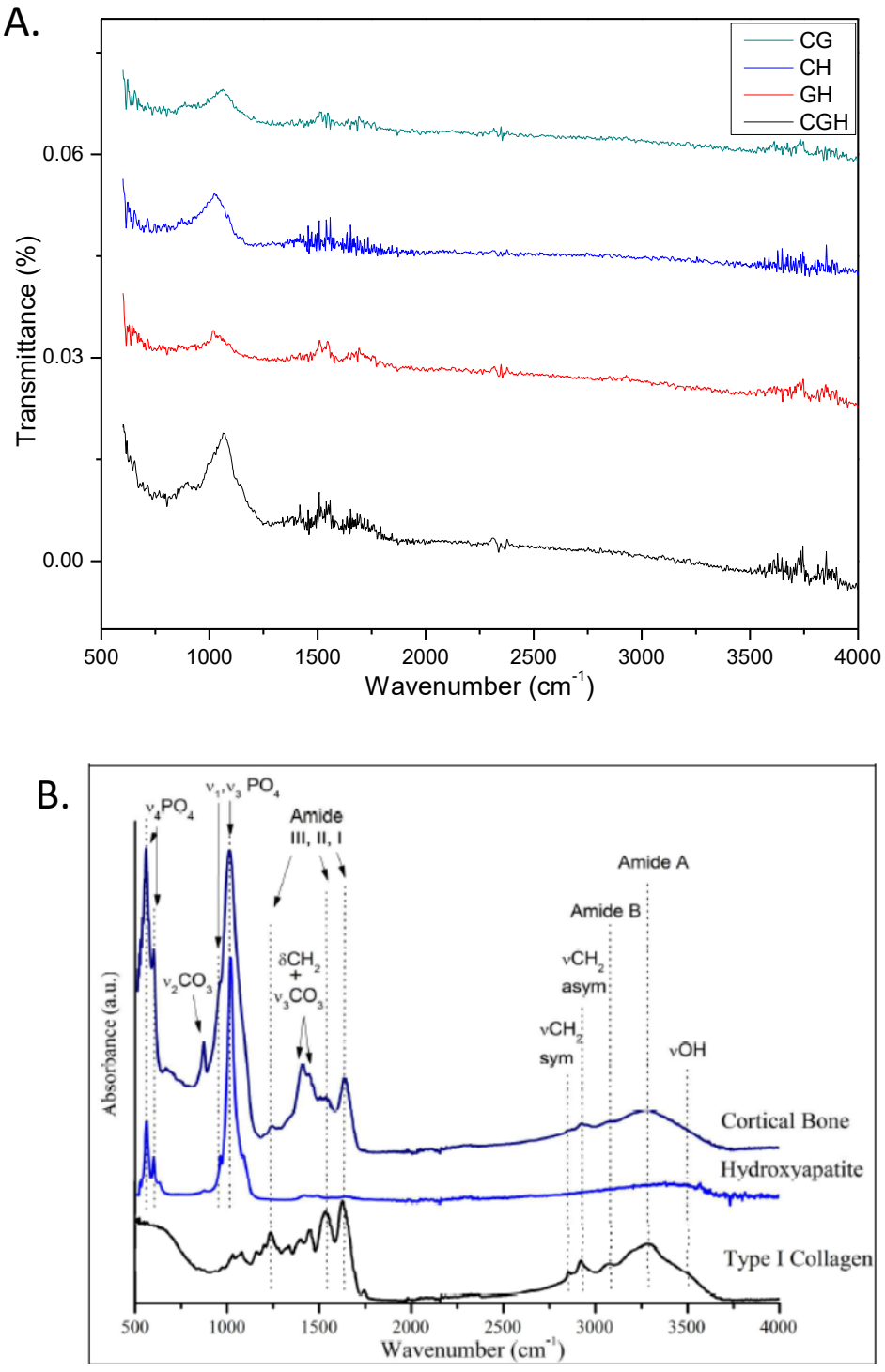

Figure 4.9 Qualitatively analyse the crystalline structure of Ca-P deposits in the scaffolds: A.(A) CG; (B) CH; (C) GH and (D) CGH. And B. The Typical FTIR spectra of bone, Ha and collagen showing the vibrational assignments of the most significant bands [209].

The relative intensities from FTIR of biomaterial before cell-seeding are summarised in **Figure 4.9**. These readings define the mineral phase deposited by cells during co-culture. The inorganic-part of the deposited mineral phase resembles inorganic-hydroxylapatite intensities [136].

Crystalline Hydroxylapatite intensities fall in a frequency range (in cm^{-1}) of 625-770, 2957 and 3250-3300 assigned to amide IV (mainly 0=C-N deformation), asymmetric CH_3 stretching and amide A (N-H stretch), respectively. All except amide IV intensity was also displayed in amorphous chitosan used for the biomaterial mold. The corresponding groups of characteristic wave numbers in the scaffold constituents listed in **Table 4.5.** FTIR peaks afirms cell attachment and mineral deposition by the osteogenic cell population [208].

Intensity / Groups	PO_4^{3-}	O=C-N		*PO_2^-	C=O of COO^-	H-O-H bend	C=O From amide I	-C=O		O-H in -COOH
	557	622	783	1119	1397	1642	1745	2068	2365	3469
#1 CH	+	+	+	+	+		-	-	+	-
#2 CG	-	+	-	+	-	-	-	-	-	-
#3 GH	+	+	+	+	+		-	+	-	+
#4 CGH	+	+	+	+	+		-	+	-	+

Table 4.5 Distribution of characteristic groups within the scaffold materials

The bands observed to be at around peak values of 1099 cm^{-1}, 952 cm^{-1}, 839 cm^{-1}, and 563 cm^{-1} corresponded to a phosphate ion (PO_4^-) from Ha. The carbonate bands around at 1457 cm^{-1}, 1433 cm^{-1} and 840 cm^{-1} also was observed.

From the chitosan spectrum [112], C-O and C=O from the ester functional group in CGH proof the contribution of chitosan.

4.1.4 Thermal study

DSC studies were carried out to know biomaterial thermal behaviour in terms of moisture content which influences their quality and shelf life. For every scaffold, the exothermic peak/s were upto 100 °C were related to the evaporation of water, and then the immediate one with the transition from the helical structure into a less ordered form. From **Figure 4.10** DSC endothermic data, the thermal stability of the biomaterials increased with the inclusion of gelatin [210].

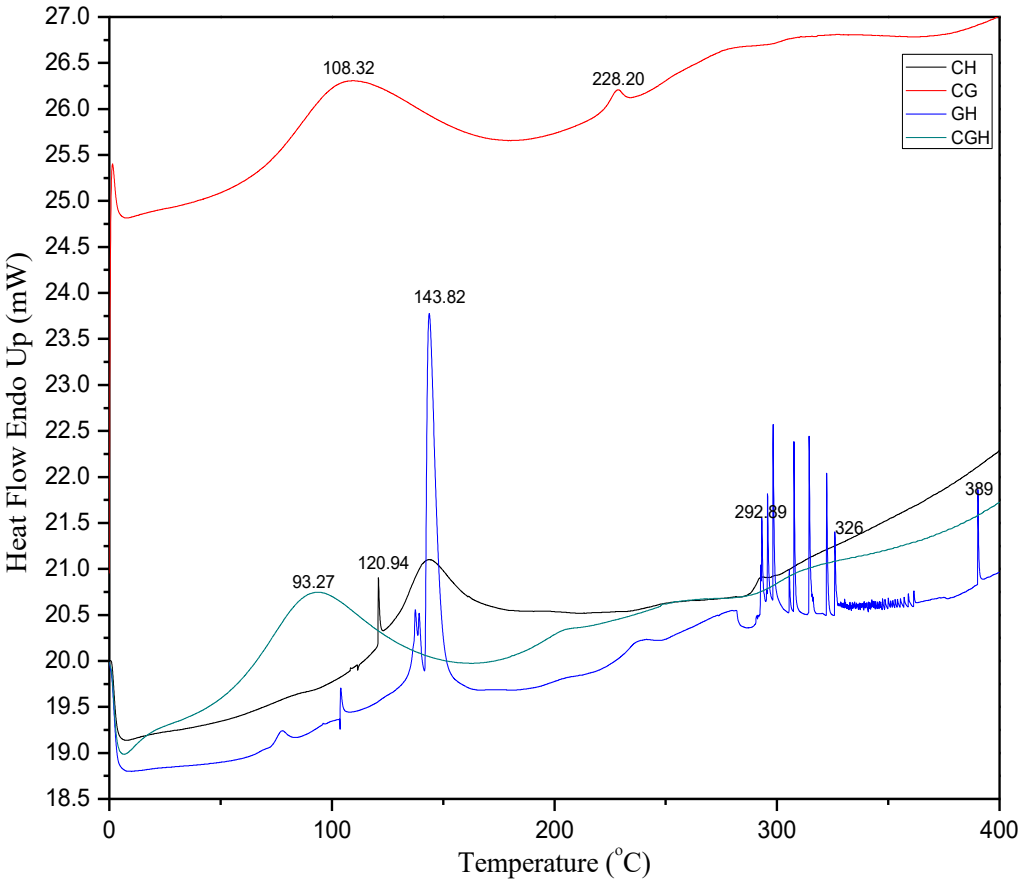

Figure 4.10 DSC thermograph of the scaffold materials namely, CH, CG, GH and CGH before cell-seeding.

Reduction in particle size of both chitosan and Ha leads to increase in surface energy and thermal stability after interaction with gelatin matrix [111]. The temperature of the transition is dependent on the degree of mineralization in turn effecting thermal stability of the polymer in the biomaterial.

The curve obtained from the scaffolds revealed the exothermic peaks, the same were listed in **Table 4.6.**

Sr. No.	Scaffold	T_g (°C)
1.	CH	93
2.	CG	108
3.	GH	120
4.	CGH	143

Table 4.6 Tg from the DSC thermogram of composites (a) CH; (b) CG; (c) GH and (d) CGH.

The Glass transition temperature (Tg) influencing the biomaterial physical poperty were observed to be 120°C, 108°C, 143°C, and 93°C for #1, #2, #3 and #4 respectively. The endothermic peak observed only in CG was associated with melting temperature of chitosan. The same being absent in GH but negligibly present in CH and CGH. The denaturation peak shifted to a higher melting temperature (Tm>300 °C). From Tg, GH displayed highest shelf life. It indicates stronger stabilizing chemical interaction between the organic and inorganic phase within the biomaterial.

4.1.5 Mechanical study

The mechanical strength favors the selection of optimal biomaterial out of CG, CH, GH and CGH for supporting ECM deposition and compressive strength, *in vitro* for bone tissue engineering [211]. From UCS study it was observed that, in the the scaffold GH and CGH stress was developed only along the direction of compression where as free expantion was observed along the diameter, also observed by S.Eftekhari et.al. [212].

It was seen that among these scaffolds CG softened as it entered the plastic stage [142]. This observation resulted in non-uniform stress distribution leading to CG scaffold failure in low-weight bearing regenerative studies.

The indentation was the highest in CH by about 54%, making it brittle for consideration. Similar results were obtained in the work of X.Peng et.al. [213]. Whereas, CG showed the maximum compression among the scaffolds studied, indicating relatively poorer mechanical strength. This was observed due to increased hydrophilicity [22].

The typical load-indentation curve for the GH and CGH scaffold are presented in **Figure 4.11**.

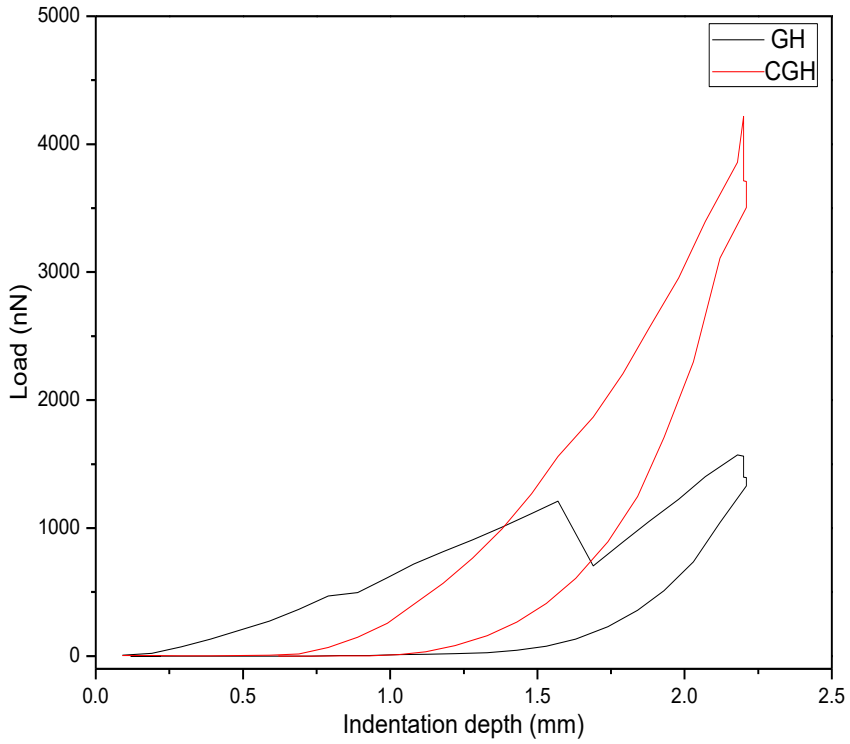

Figure 4.11 Uniaxial Compressive Strength measurement of the scaffolds GH and CGH

From **Figure 4.11**, the calculated Uniaxial Compressive Strength (UCS) (for n=5) and average of the result has shown improved compressive strength with chitosan introduction in GH [214]. This rise in UCS suggests gelatin can improve ECM

mineralization without majorly affecting the mechanical strength. The stiffness of the biomaterial increased from 1 to 20 kPa upon gelatin introduction also observed before [108].CGH showed increased stiffness over GH notably due to stronger bending vibrations as also noted from FTIR. From the records, compressive strength of the scaffold found to have a relation with the chitosan content in those scaffolds. The reduction in the degree of mechanical strength may be due to the increase in Ha in matrix resulting in inability of matrix to bear the increased Ha proportion, resulting in decrease in the mechanical strength was also reported [113, 215]. This also supports chitosan introduction causes decrease in flexibility of the biomaterial [216]. Among the scaffold materials, the torsional strength of intact bone, with a maximum torque of 20±0.558 Pa was achieved in CGH.

Sr. No.	Scaffold	Young Modulus (Pa)
1.	CH	$15.3x10^5$
2.	CG	$-0.11x10^5$
3.	GH	$11.22x10^5$
4.	CGH	$20.54x10^5$

Table 4.7 The young's modulus defining the mechanical strength of the respective scaffolds.

From the **Table 5.7**, the Ha introduction resulted in reduced compressive strength when present with either chitosan and gelatin as CH and GH, respectively [50]. However, brittle Ha's stiffness was balanced by both chitosan and gelatin together following interaction in CGH. For all of the four scaffold groups (namely CH, CG, GH and CGH), the average strength fell in the range same as for cortical to cancellous bone between 2 MPa-20 GPa [217]. Also, refer to the value of Young's modulus in Table 4.7. The elastic modulus was

closer to that of the cancellous bone [218]. The scaffold rigidity and spatial architecture determines the mechanical behavior of the scaffold which in turn regulates the cell's response (proliferation and ECM rigidity). Furthermore, the cortical stiffness for rM have shown to increase above 20 KPa and cell surface were stable around ~10 KPa. The scaffold mechanical property made them to be the likely candidates for bone tissue regenerative application.

4.1.6 Porosity

A porous architecture improves the mechanical interlocking of the implanted scaffold with the surrounding host bone. The stiffness and mechanical strength increases as the porosity decreases, was also confirmed by the scaffolds based on calcium phosphate [80,219]. Moreover, enhanced mechanical strength resulted from the thickened pore walls and reduced scaffold porosity.

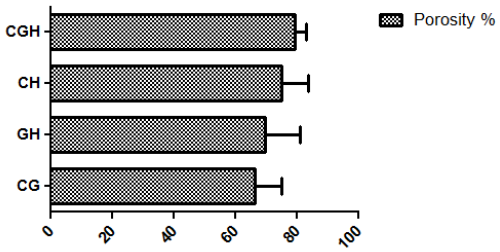

Figure 4.12 Porosity defined for the scaffolds: CGH, CH, GH and CG.

For the desired variation of porosity of the scaffold for bone growth, in this work from **Figure 4.12** the scaffold porosities were calculated to be in the range from 70-90% as observed for all of the scaffold materials i.e. CH, GH, CG and CGH. All of the scaffolds presented porous architecture with pore size spanning 250-300 µm [144]. This range had been recommended for enhanced new bone formation in the previous literature [132]. The gelate-freezing process showed cell-structure with high compressive strength and high porosity in comparison to the other processing methods [195].

Figure 4.12 presents increased porosity for CGH. Highest concentration in CG resulted in reduced porosity a thick pore walls, however, plastic nature of CG resulted in poor mechanical strength too. For the remaining scaffolds the results of mechanical properties were consistent with the porosity studies of the scaffolds. The key determinants for the scaffold to be suitable for lineage specification in MSCs had been the pore size and substrate stiffness, they were known to influence the cellular adhesion, infiltration and proliferation.

4.1.7 Degradation and mineralization

4.1.7.1 Degradation

The osteoblast proliferation and expansion after cell seeding on the scaffold was affected by the balanced degradation-to-mineralization ability of that scaffold. **Figure 4.13** illustrates the effect of 'lysozyme in DPBS' induced degradation of the biomaterial for a month when kept under physiological conditions. Scaffolds with hydrophobicity favouring the degradation rate appropriate for bone tissue engineering applications were to be selected for further *in vitro* studies. Every biomaterial degraded linearly during this degradation period (~10-15% every week) [220]. The increase in weight loss percentage of CG was more than the other biomaterials where CGH displayed step-well degradation of 80% till culture day 30. This indicates ability of hydroxylapatite in sustaining the biomaterial longer in culture duration [221]. The CH biomaterial degraded more than CGH [152,222].

This observation indicated the role of gelatin in modifying the degradation period. For instance, some degradation was evident in CG after 3 weeks of implantation in a femoral defect model in spite of mass loss was only around 9% when the scaffold was immersed in Lysozyme in PBS, *in vitro* [117].

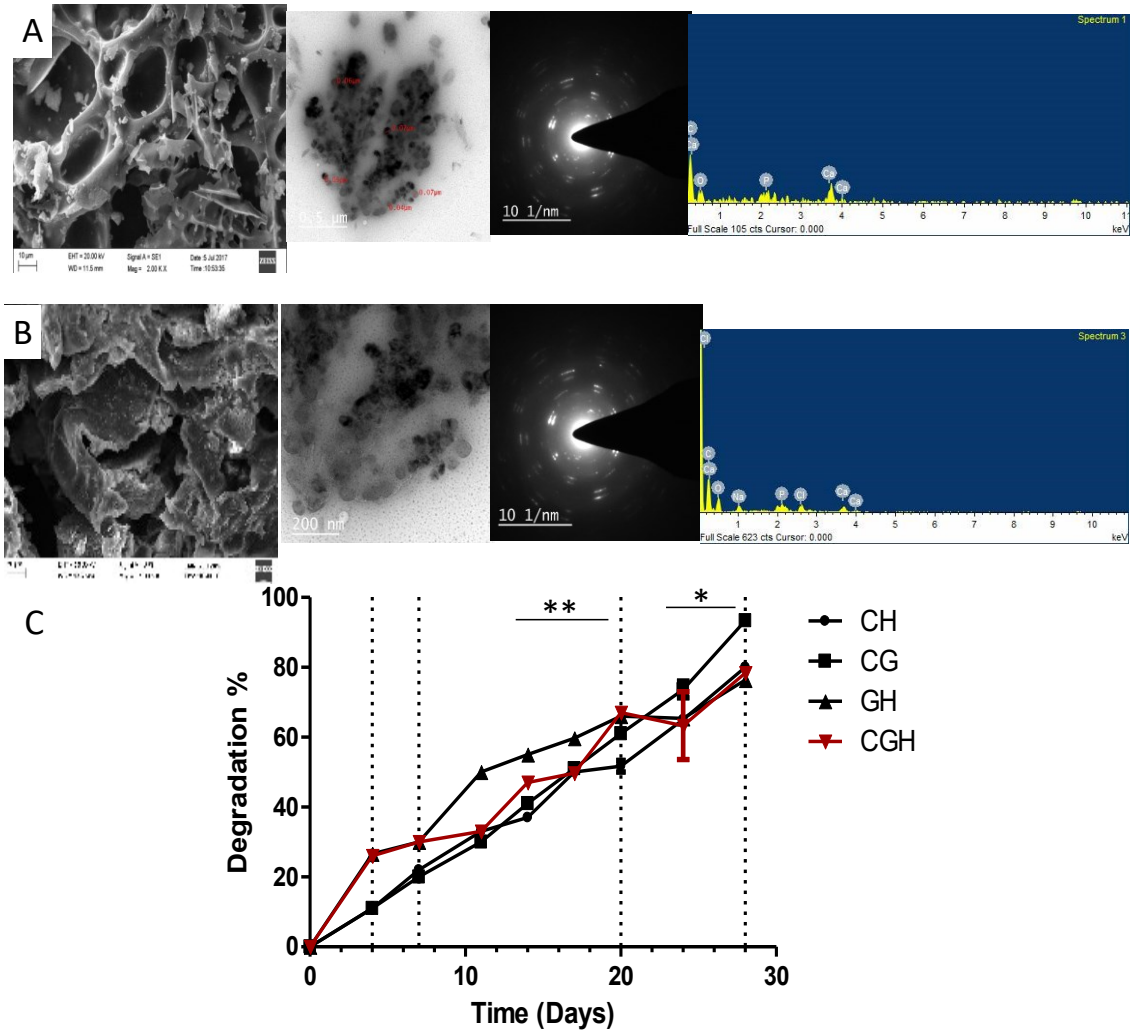

Figure 4.13 SEM, TEM-SAED images of composites (a) GH and (b) CGH showing (c) degradation as a function of time after immersed in lysozyme. **P<0.01, *P<0.0001.

The scaffolds were considered stable as no elemental modifications were noticed after 28 days of incubation. Over the incubation period the DPBS pH remained unchanged, indicating absence of acidic degradative byproducts. From the lifetime of scaffolds in lysozyme *in vitro*, noticeable mass loss was found for CG immediately within 1week of incubation. This facilitated in estimating the scaffold lifetime *in vivo* in the range 1week to 1month. However, the time-points have to be confirmed from longer in vivo studies.

Ha contributed towards poor degradation whereas gelatin promoted degradation [102]. This may be due to the decrease in the accessibility of enzyme to the hydrophilic groups of the Ha. The degradation rate could be adjusted by controlling the fraction of different scaffold raw materials.

4.1.7.1 Mineralization

The ability of biomaterials in promoting mineralization under physiological conditions was tested in 1.5 X simulated body fluid (SBF) solution. This mineral deposition noted from culture day 14 in all the biomaterials using SEM and TEM-SAED in **Figure 4.14**. The bone-apatite deposition on the material's surface is proportional to the increase in bioactivity. The deposition led to increase in the crystalline nature of CGH after culture day 14 thereby improving its *in vitro* bioactivity. The percent mass increase was from 20-40% the initial after about 4 weeks in SBF. This attributed mainly from creation of mineral nucleation site to favouring bone-like apatite growth in the biomaterial [223].

The percent mass increase was noted to be significantly higher in CGH than the other scaffolds. After 1 week in SBF, the percent mass increase followed similar trend for both GH and CG. The trend was linear for CH, while step-well for CGH. In the same time-interval, more apatite was deposited in CGH. With minimum rise in mineralization reported for CG, indicating role of Ha in promoting bioactive behaviour when co-exist with either chitosan or gelatin or both.

The absence of apatite component lead to minimum deposition in CG biomaterial and hence reduced bioactivity and bone-bonding ability [102].

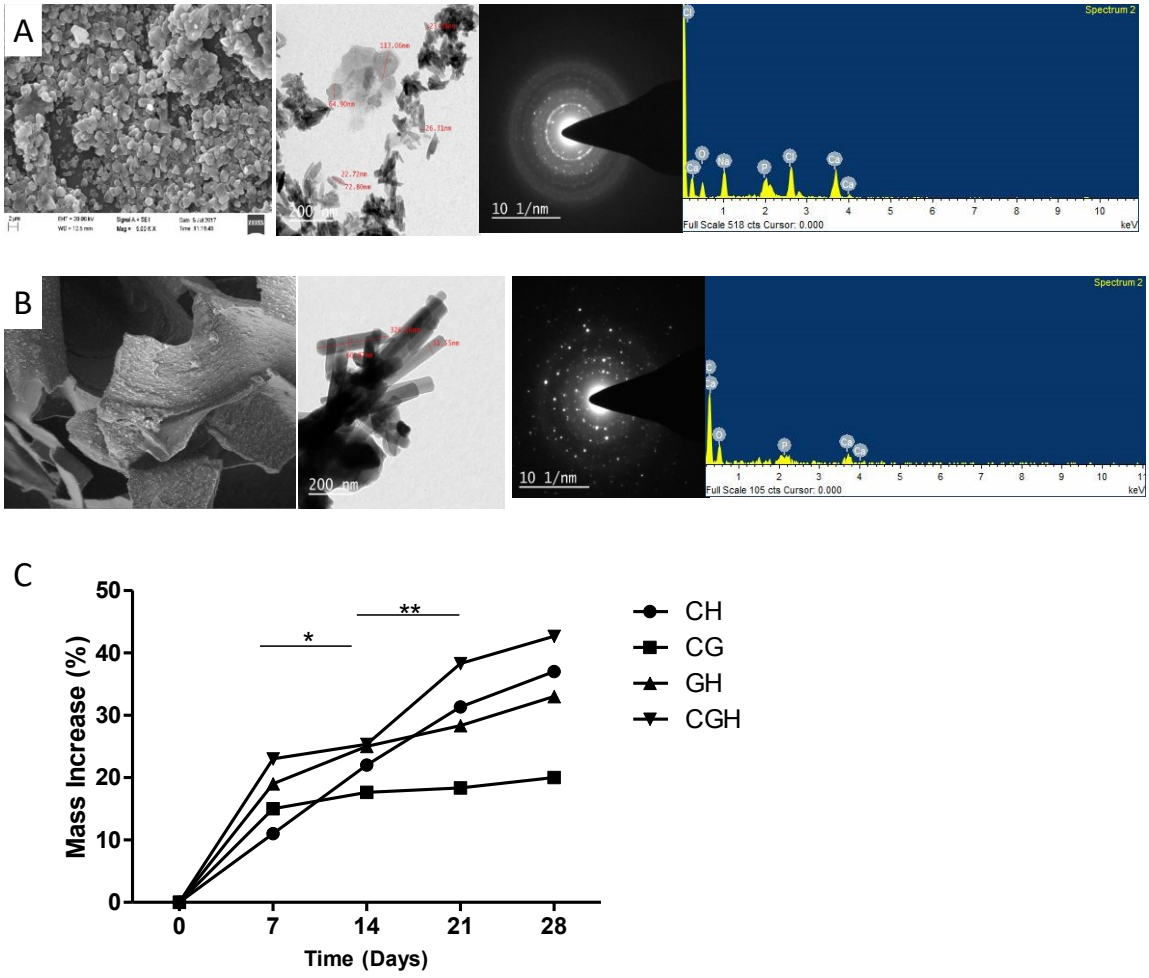

Figure 4.14 SEM-EDX, TEM-SAED images of composites (a) GH and (b) CGH showing (c) mineralization as a function of time after immersed in SBF. **P<0.01, *P<0.0001.

In **Figure 4.14A-B**, the SEM images confirmed the formation of bone-apatite on the GH and CGH surface. From **Figure 4.14**, the increase in crystal spots observed from SAED data for CGH too. EDX-spectrum favoured the increase in calcium enriched deposition. The resultant percent mass increase due to inorganic minerals deposited in the scaffold pores was in the order of CGH>CH>GH>CG. The presence of both Ha and chitosan, within gelatin matrix resulted in decrease in the surface energy for mineral nucleation on the CGH scaffold. Both indicated to have synergistic effect in inducing apatite formation and deposition resulting in enhanced bioactivity of CGH closely followed by CH.

4.1.8 Innate Antibacterial Activity assessment

From **Figure 4.15**, CGH is displaying antibacterial nature towards both gram positive and gram negative bacterium.

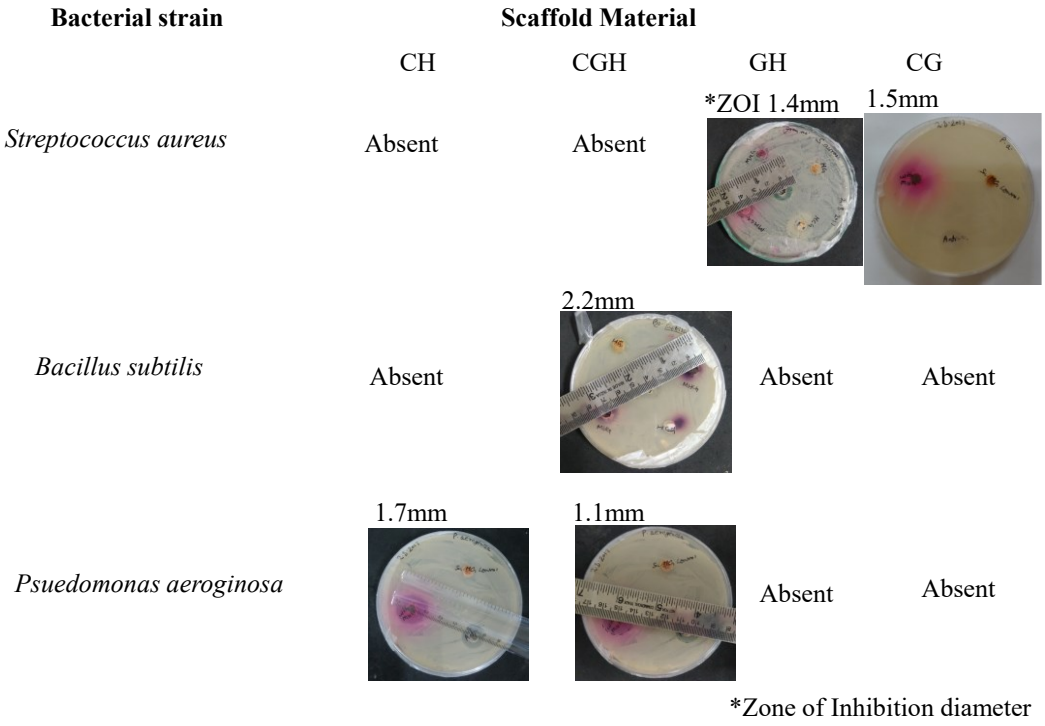

Figure 4.15 Comparative display of innate antibacterial activity of scaffold materials studied *in vitro,* namely CH, CGH, GH and CG.

In the presence of CH, the growth of gram negative *P.aeroginosa* was inhibited but not gram positive. Whereas, in the presence of wither GH and CG the growth of gram positive *B.subtilis* was inhibited.

In this work, the antibacterial activity against *S.aureus*, *B.subtilis* and *P.aeroginosa* was screened by the agar diffusion method [224]. From the inhibitory halo seen around the CGH scaffold it can be revealed that the CGH promoted the inhibition of *B.subtilis* and *P.aeroginosa* growth (**Figure 4.15**). The highest bactericidal effect was presented from the largest inhibitory zone (around 2.2 cm diameter), as demonstrated in **Figure 4.15**.

Chitosan, used for the scaffold fabrication, can prevent nutrient exchange on bacterial surface by creating a barrier. Chitosan leads to increase in the bacteria cell wall permeability, dissipating the intracellular ionic gradient [222].

Thus, these scaffolds effectively prevent the defect site from being exogenously infected for initial 7 days, which was critical for progressive wound healing [225,226]. In conclusion, the results showed that CGH scaffold has good antibacterial activity against both gram positive and negative bacteria.

From the scaffold-based study it was observed that the effect of 'Ca-P present on the surface as coating' on the proliferation of the seeded-cell depends on the Ca-P mineral phase, crystallinity and the degradation pattern of the scaffolds.

The investigated characteristic properties have proved the potential of both GH and CGH, to be considered as a temporary substrate for bone tissue engineering.

4.2 Rabbit cell study

4.2.1 MSC identification

Surface molecules expression in primary cells was evaluated for MSCs identification [184]. The MSC population was distinctively identified during isolation by the specific surface antigen expression in MSCs by flow cytometry in **Figure 4.16**, i.e. positive for CD90, CD 73, CD 105 and negative for CD34 and CD 45 [227,228].

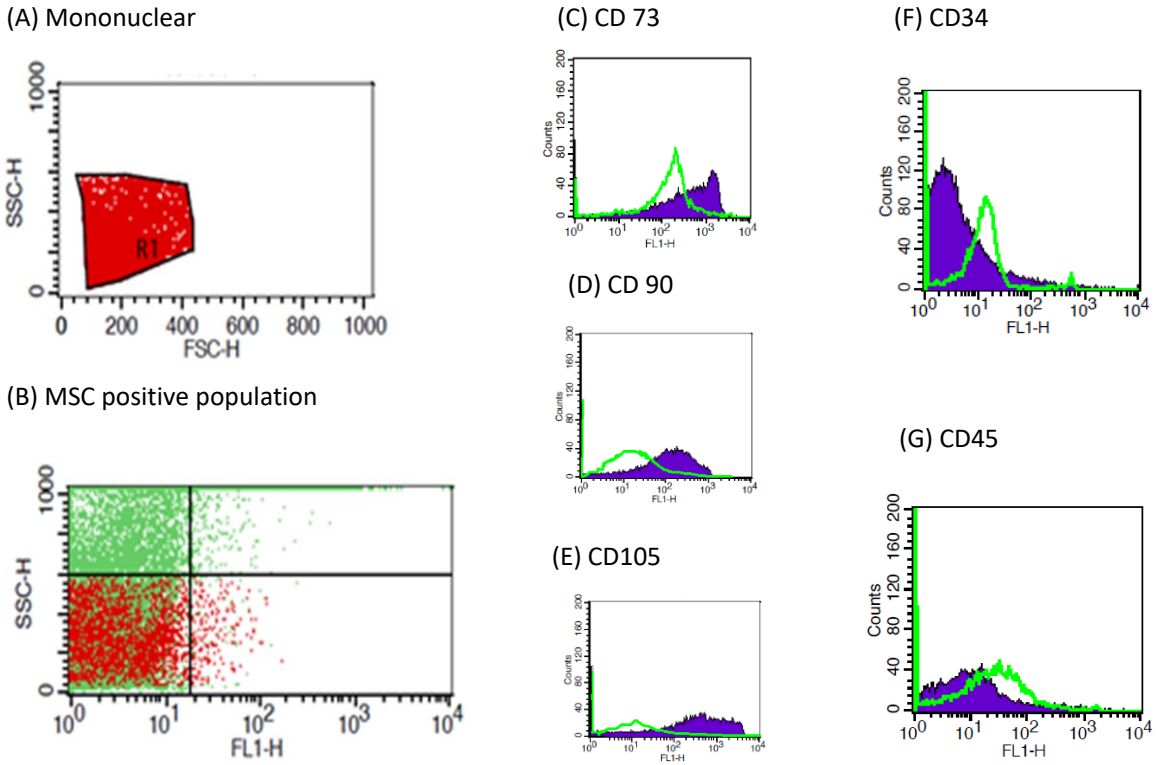

Figure 4.16 Histograms from flow cytometry analysis of cell surface markers for MSC identification from the bone marrow (A) Dot plot before sorting, (B) Dot plot after sorting, (C) CD73 positive fraction after sorting, (D) CD90 positive fraction after sorting, (E) CD105 positive fraction after sorting, (F) CD34 positive fraction after sorting and (G) CD45 positive fraction after sorting.

**CD- cluster of differentiation as cell surface markers.*

** FITC- Fluorescein IsoThyoCyanate*

While low level of CD34-expressing cells indicate haematopoietic cells, which were positive for CD 34. Taken together, Figure 5.16 have shown a good level of CD73, CD90 and CD105-expressing cells in rabbit MSCS in the mono-nuclear population.

Freshly isolated rabbit bone marrow mononuclear cell population were stained with antibodies (CD73, CD90 and CD105) to be analysed by flow cytometry. The representative cell count from both positive and negative selection were plotted. The MSCs expressing the indicated marker were shown after forward/side scatter gating, exclusion of dead cells (PI), and gating on CD34 and CD45 cells [229]. Solid indicate the expression of the marker listed on top and green line indicate the control population not expressing the respective marker. The FACS plot shows one representative set for a total of five independent experiments.

4.2.2 Cell cycle analysis

A cell cycle overlay plot with both the cell types were used for this study, namely rM and rT and displayed in **Figure 4.17**. This overlay depicts cell count distribution over the cell cycle phase. It determined the fraction of cell population for cell seeding. G0/G1 phase population was chosen for cell-seeding for both the cell types. The FACS data has shown that fraction of the rM and rT cells seeded on both scaffold materials were in S phase of the cell cycle (**Figure 4.17B**). Furthermore, the cell cycle analysis revealed that the majority of the cumulative CD105+, CD73+ and CD90+ cells were in the G_0 phase of the cell cycle.

(A) Cell Cycle Overlay

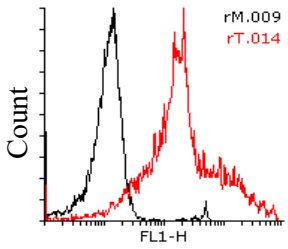

(B) Cell distribution of rM and rT

rM	Events	% of Vis	Mean	GeoMean	Median	CV
All events	10,000	100.00	18.91	10.25	11.55	293.02
G0/G1	2,577	25.77	12.98	12.93	12.98	8.64
S	2,593	25.93	20.13	19.33	18.11	40.16
G2/M	14	0.14	178.53	177.71	173.09	9.64
rT	Events	% of Vis	Mean	GeoMean	Median	CV
All events	10,000	100.00	510.10	185.39	181.06	184.66
G0/G1	7,978	79.78	262.12	180.43	176.24	96.21
S	697	6.97	1,739.41	1,704.63	1,700.08	20.29
G2/M	431	4.31	4,140.94	3,934.11	3,718.03	33.56

Figure 4.17 Cell cycle analysis of the rabbit osteoblast isolated from the bone tissue (rT) and osteoblast obtained after differentiation of Mesenchymal stem cells from bone marrow (rM): (a) Cell Cycle overlay and (b) Cellular distribution.

4.2.3 Growth curve analysis

The growth curve depicted three distinct phase namely lag, exponential and plateau. Both the cell line exhibited the lag phase of 36-48h. The exponential phase of 4-6 days occurred quickly for rM followed by rT. The exponential phases was comparable, it was extended in rT whereas shorter in rM. rT grew rapidly and had lower population doubling time (PDT) resulting in higher clonogenic potential and hence faster expansion. In general agreement with the MSCs behaviour, rM had longer PDT when in monolayer.

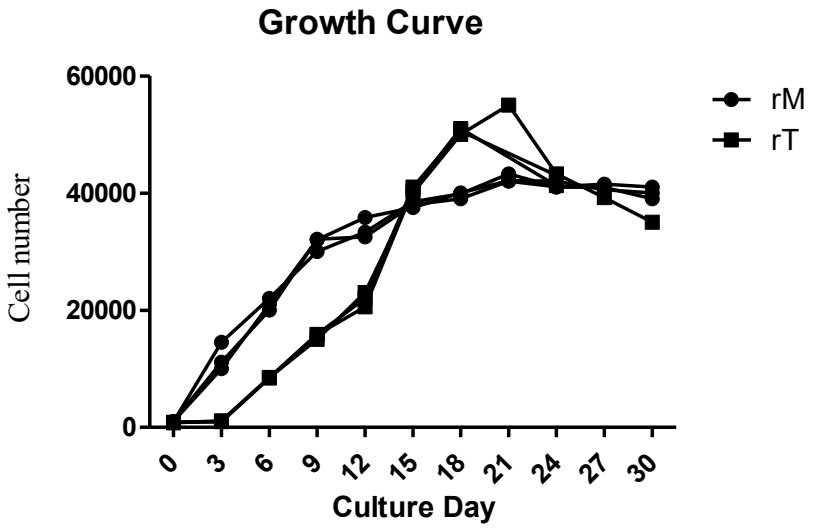

*rM-Osteoblast differentiated from isolated Mesenchymal Stem cell from rabbit Bone Marrow &
rT- Osteoblast obtained from Rabbit iliac crest bone tissue

Figure 4.18 Growth curve analysis of rT and rM.

4.2.4 *in vitro* cell morphology, attachment and proliferation

Each of the isolated cells when seeded in the CGH scaffolds displayed spherical shape shortly after seeding. After 24-48 h, the majority of MSCs became adherent by displaying different morphology, predominantly polygonal and the large nuclei were located near the margin of the cells. Figure shows confocal micrograph of rM and rT on both GH and CGH after culture day 14. Scattered fibroblast-like shape are observed after cell culture in GH scaffold (**Figure 4.19**).

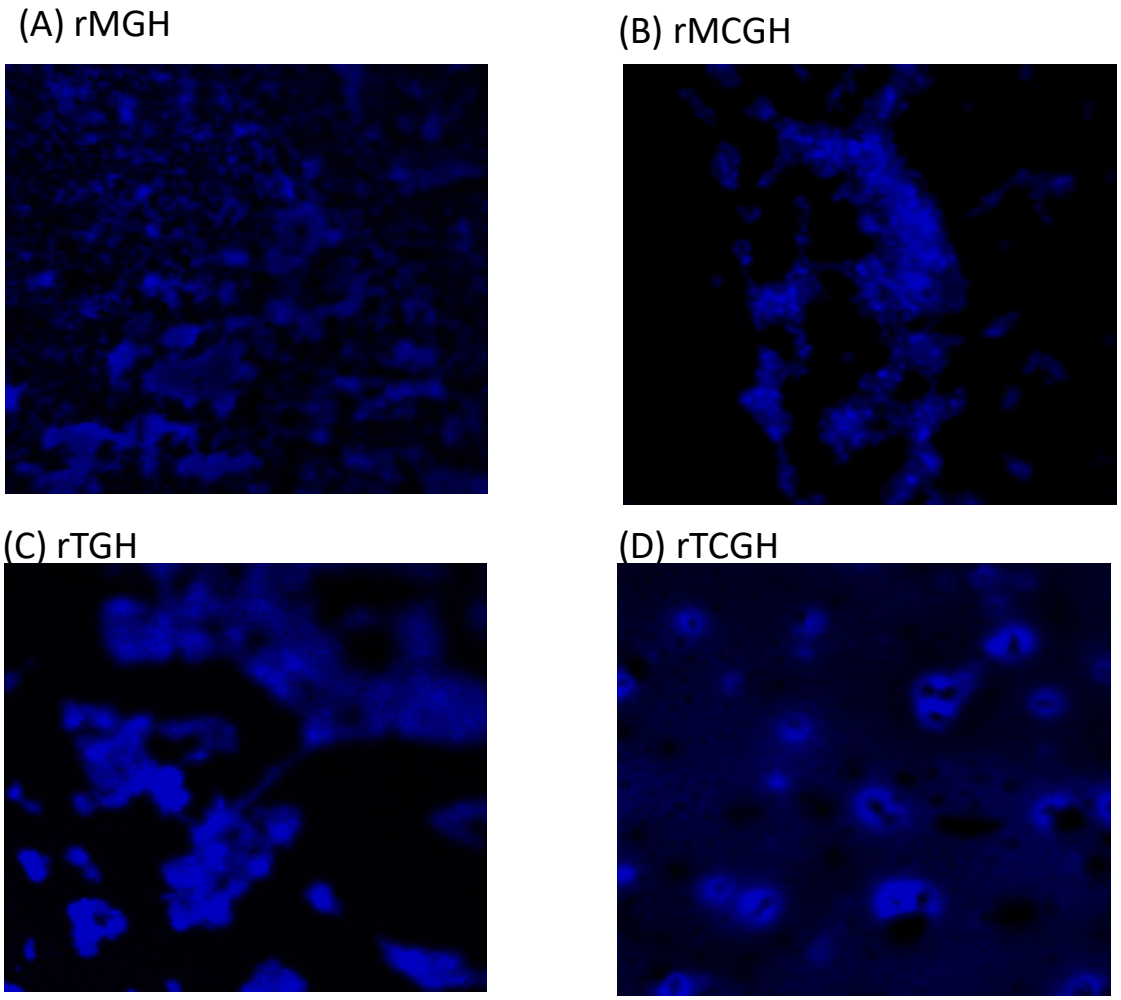

Figure 4.19 Effect of scaffold on the biological response of cells studied *in vitro* by **CLSM.** Hoechst 33258 labelled images of both the cell and the four scaffold composites after cell seeding: (A-E). Magnification (63X).

Confocal images revealed that a large number of cells were adhered to the scaffolds. Profuse cell proliferation was observed in the cell seeded scaffold materials by CLSM has also been reported in previous work [230]. Morphology of rOb and experimental group was observed using Hoechst 33258-nuclear staining and alexa fluor 488-ECM staining from culture day 14 scaffolds. Cells on GH is showing prominent adherence while CGH group is showing well-spread smooth cell morphology (**Figure 4.19**).

Cell adhesion to the scaffolds was previously reported in the literature, using osteoblasts from differentiated MSCs, indicating the osteogenic potential of the scaffolds [231].

Cell densities increased with the gain in the cell culture time on the scaffold along with the cytoskeleton synthesis by mainly rMGH and rTCGH over rMCGH and rTCGH. In CGH, rM cells initially presented a round morphology (Figure 5A) and with time became elliptical whereas rT presented polygonal morphology and then after spread well on the scaffolds (**Figure 4.19A-D**). These results clearly reveal that rM took longer duration than rT to attach to CGH surface and proliferate, whereas both the cell types spread with gain in cell culture duration.

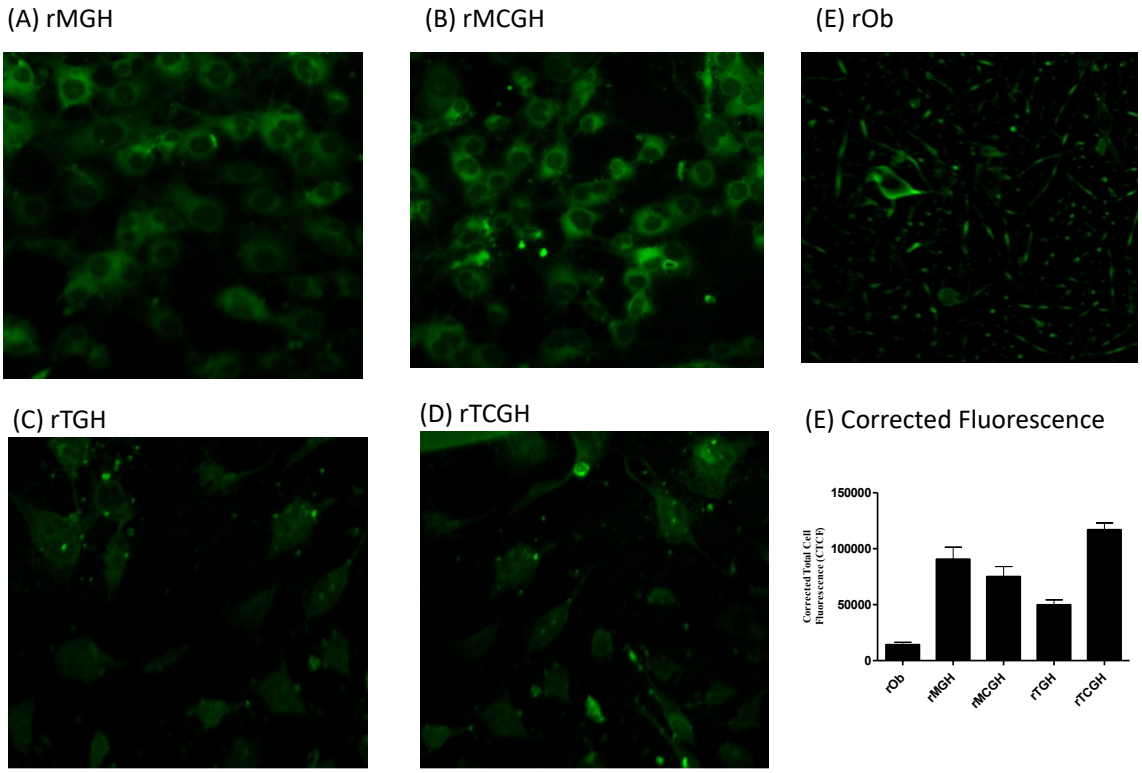

Figure 4.20 CLSM Images of Alexa fluor 488 labeled four composites after cell seeding: (A-D) and the E.Corrected Fluorescence. Magnification (63X).

Figures 4.20B-E shows cells within the uniform well spread interconnecting cytoskeleton network. The increasing numbers of cell extensions from the ECM of rM were evident [232]. A higher degree of multiple cell-cell contacts signal cell spreading events in favour of the extensive networks of ECM. This result revealed higher proliferation and spreading of rT over rM after 14 days of cell culture in CGH over GH.

Figure 4.21 and Figure 4.22 shows flow cytometry analysis of the cell morphology and cell density after culturing rM and rT in GH and CGH for 28 culture days. The Purity of isolated unstained rM and rT fraction was 76.3% and 41.1%, respectively. These results displayed the possibility of discriminating the monolayer expanded rM cell population from the rM culture in the 3D scaffolds GH and CGH.

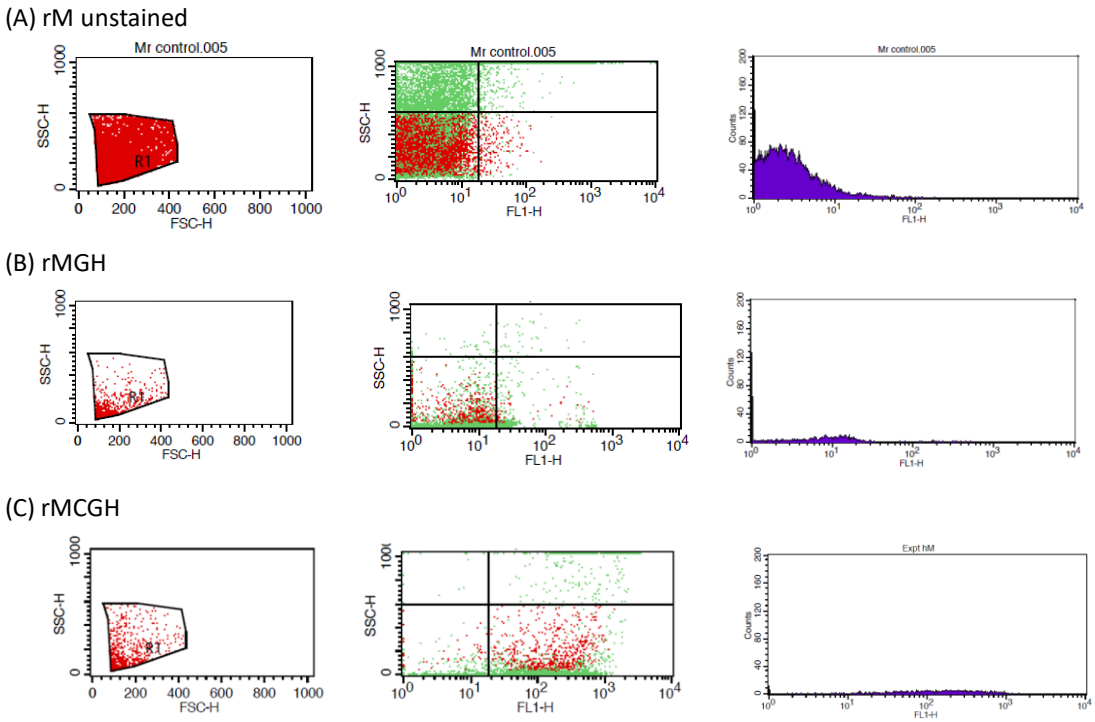

Figure 4.21 Dot plots and cell count from the flow cytometric analysis of rM (A) when cultured in monolayer and (B-C) cultured in the scaffolds GH and CGH.

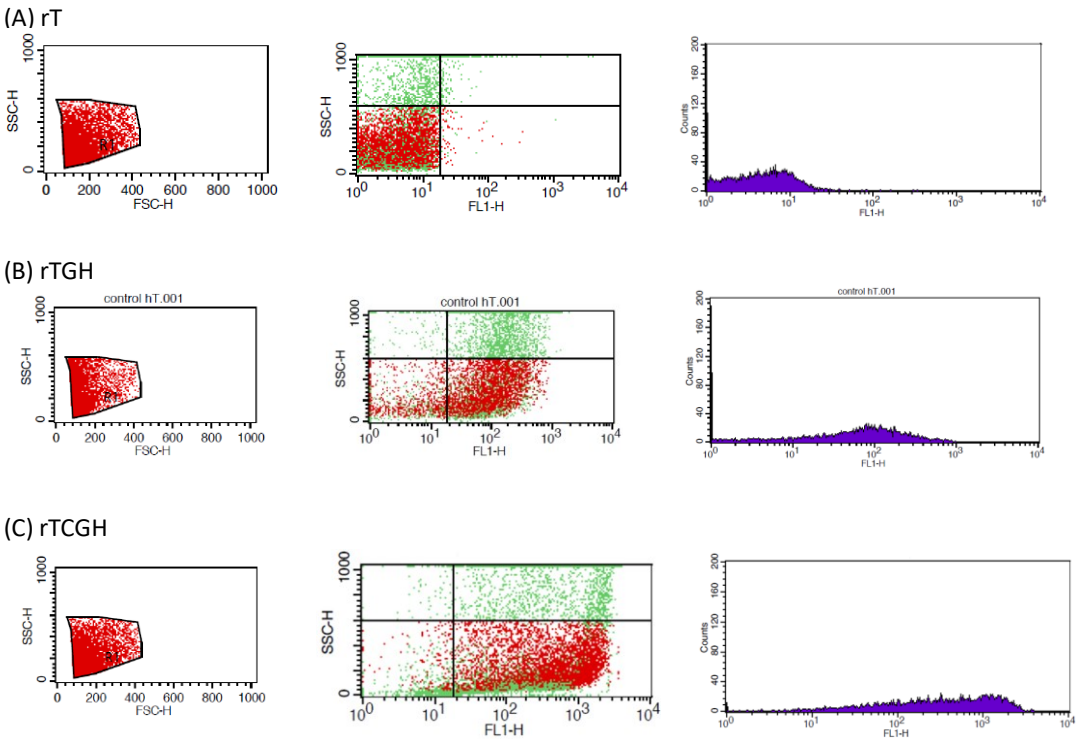

Figure 4.22 Dot plots and cell count from the flow cytometric analysis of rT (A) when cultured in monolayer and (B-C) cultured in the scaffolds GH and CGH.

4.2.5 Morphology Characterization

4.2.5.1 Surface morphology

Gelatin has shown to represent an interesting platform in designing scaffold microarchitecture, favouring invasive medical procedures. These were able to withstand major bone deformations when supported by the inorganic component, also reported in the previous work done [55,121].

To understand the role of scaffold material's surface morphology followed by core morphology, as the crucial parameter for osteoblast attachment and spreading as followed by ECM mineralization enable the selection of scaffold materials suitable for bone tisue engineering.

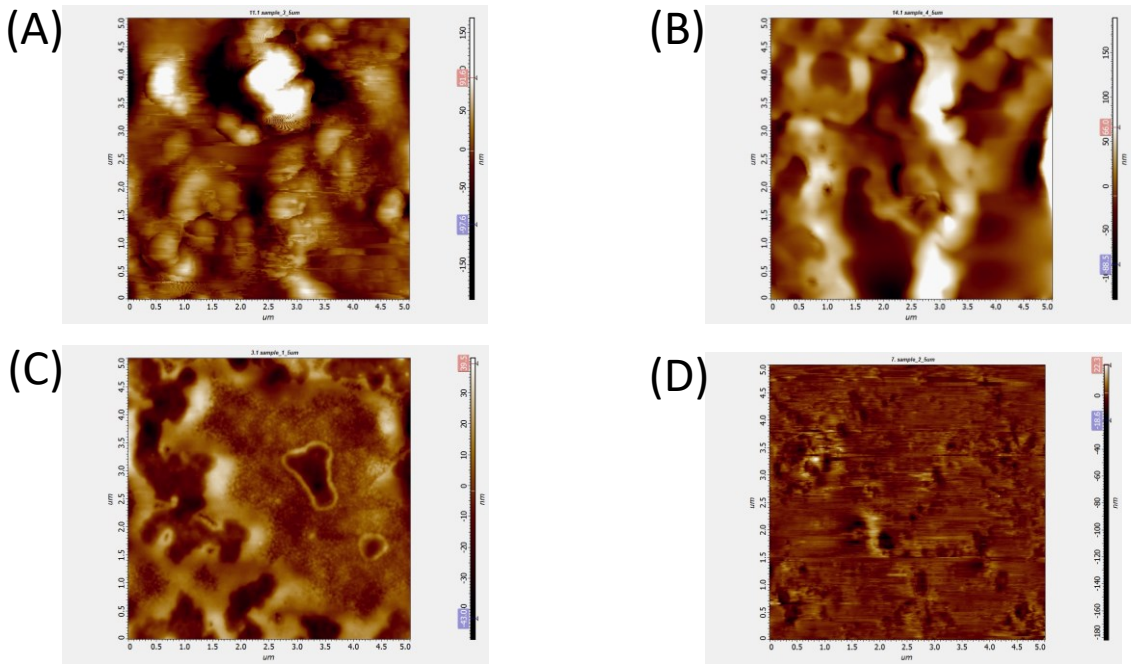

Figure 4.23 Surface topography of cell seeded composites observed in the AFM spectrum: A. rMGH. B. rMCGH, C. rTGH. D. rTCGH (Scale bar 5µm).

From AFM in **Figure 4.23**, the globular chains are surrounded and embedded in the ECM also observed on the surface of the scaffold materials seeded with rM. It is indicative of the prominent aggregate forming nature of the scaffold materials after seeding with rM. Whereas in the scaffold materials seeded with rT, the matrix surface displays distinct particle due to similar aggregates on the scaffold materials surface promoting cell proliferation and Ca-P adsorption. These results are in agreement with the previous work reported [233] in reference to the cellular distribution.

Sr. No.	Sample	Roughness average (nm)	Skewness	Grain size(μm)
1.	rMGH	0.186	-0.469	0.0527
2.	rMCGH	4.618	0.357	0.012
3.	rTGH	0.521	0.0227	0.911
4.	rTCGH	2.510	-1.315	0.0141
5.	GH	0.111	0.952	0.436
6.	CGH	1.787	0.528	0.11

Table 4.8 Surface roughness paramaters for GH and CGH scaffolds were compared both before and after cell-seeding.

From **Table 4.8**, the surface roughness parameters for the scaffold materials are comparable. The distinct roughness was noted on the denser surface of 'CGH', which had promoted calcium in protein-matrix adsorption and cell proliferation as compared to the relatively smoother surface of 'GH' which had supported maximum cell attachment. The surface roughness from AFM had shownd increased surface roughness upon chitosan introduction in GH.

4.2.5.2 Core Morphology

It was observed that core morphology changes occured in the culture day 21 in the scaffold materials pre and post rOb co-culture from SEM-EDX data.

(A)

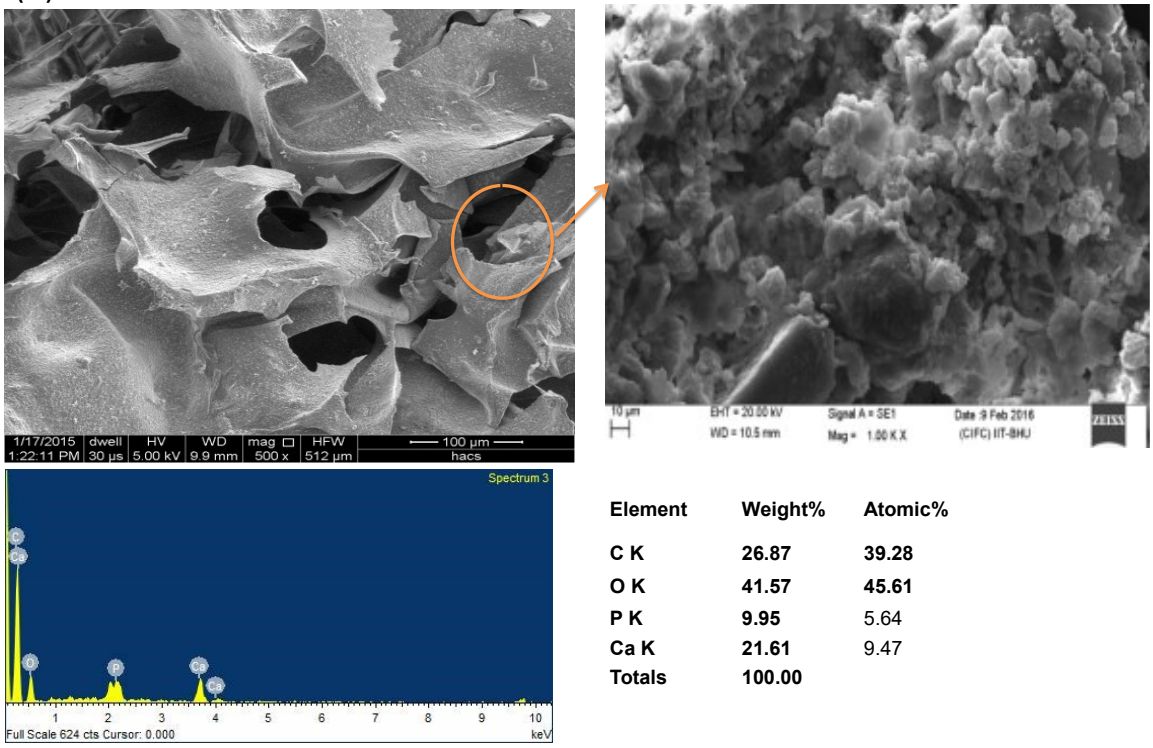

Element	Weight%	Atomic%
C K	26.87	39.28
O K	41.57	45.61
P K	9.95	5.64
Ca K	21.61	9.47
Totals	100.00	

(B)

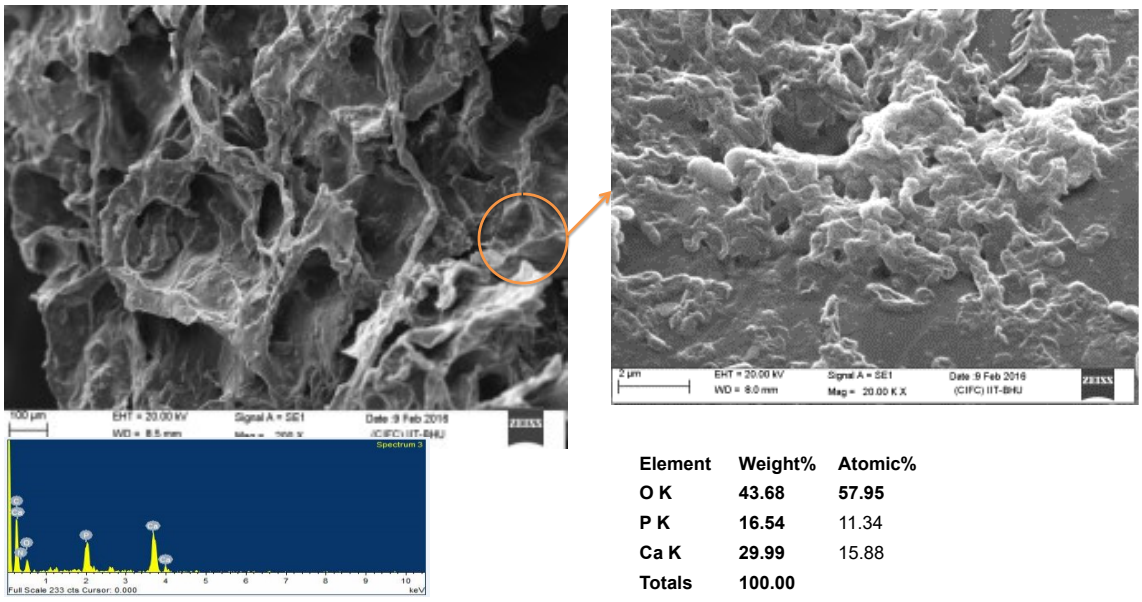

Element	Weight%	Atomic%
O K	43.68	57.95
P K	16.54	11.34
Ca K	29.99	15.88
Totals	100.00	

Figure 4.24 Pore Morphology and elemental percentage of the composites GH and CGH 21 days after seeding with rM: (A) rMHG, (B) rMHCG. (Scale bar 100 µm).

**Mineralization displayed in the inset picture of the framed area in the experimental groups (*10 µm).*

Figure 4.24 and **Figure 4.25** shows SEM images of cell-scaffold at culture day 21 in osteogenic medium.

(A)

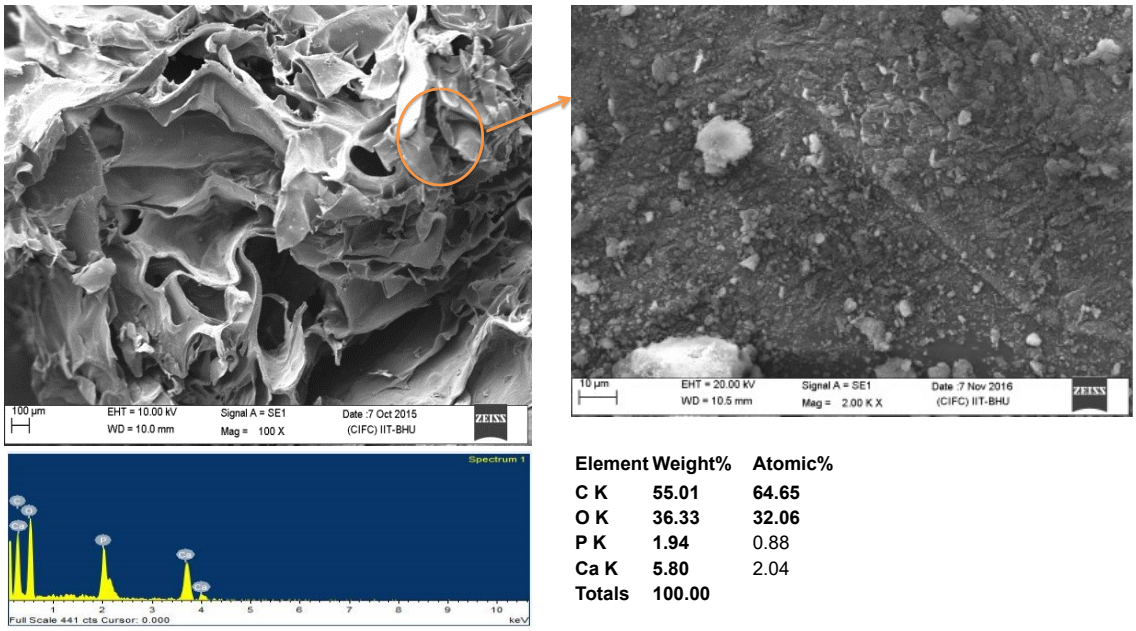

Element	Weight%	Atomic%
C K	55.01	64.65
O K	36.33	32.06
P K	1.94	0.88
Ca K	5.80	2.04
Totals	100.00	

(B)

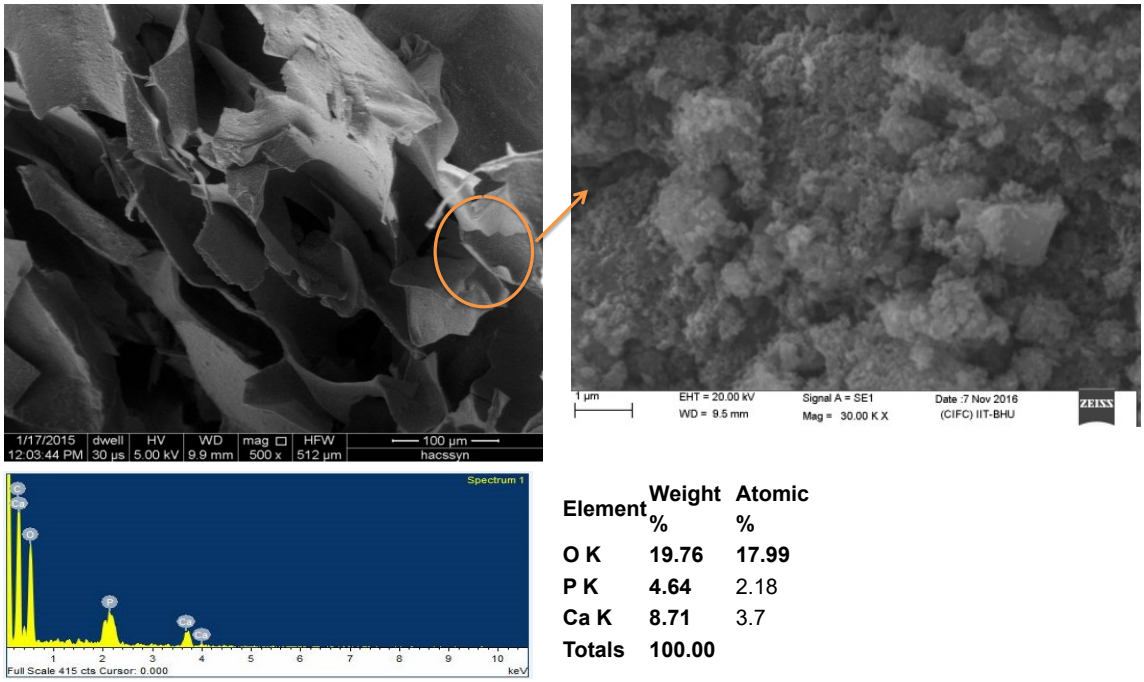

Element	Weight %	Atomic %
O K	19.76	17.99
P K	4.64	2.18
Ca K	8.71	3.7
Totals	100.00	

Figure 4.25 Pore Morphology and elemental % of the composites GH and CGH 21 days after seeding with rT: (A) rTHG and (B) rTHCG. (Scale bar 100 µm).

**Mineralization displayed in the inset picture of the framed area in the experimental groups (*10 µm).*

From the micrograph, it can be seen that both rM and rT cell types penetrated into the seeded scaffolds namely, GH and CGH. All osteoblast seeded scaffold materials showed homogeneous distribution of cells although the pattern was distinctively visible in cells seeded on GH. Aggregates with relatively smooth edges were seen in CGH whereas rough in GH as projections. Moreover, homogeneous distribution was evident throughout the entire scaffold following *in vitro* culture. The mineralization is shown in the 'inset image' and crystal deposition covering the CGH scaffold can be distinctively observed for both rMCGH and rTCGH. The retention of cells and attachment to the pores was compared between the 3D scaffold [215,234].

Coarse gelatin sphere allowed the production of scaffold with a defined spherical architecture of the pores[95]. This finding is in accordance with previous work reported [235]; however, published work mentioned improved equal contribution of chitosan in framing scaffold pore morphology both on the surface and scaffold core [236,237]. Little contradictory study result from the difficulty in the penetration and distribution of ECM produced by osteoblast within the micropores of the scaffolds reported [238].

4.2.5.3 Elemental Mapping

The EDX spectrum of the SEM images of the seeded scaffolds were sectioned and observed that it supported visible CaP (calcium phosphate) cuboid-crystal deposition on both the scaffold materials i.e. GH and CGH by culture Day 21, also prominent in CGH. Before cell seeding, Ca/P of GH (1.77) was observed to drop to 1.69 upon Chi introduction as in CGH. Identical drop in Ca/P was noted after cell seeding (**Table 4.9**). Due to the highest Ca/P, an earlier visibility of crystals noted in rTCGH. The Ca-P coating influences the cell proliferation by effecting the mineral phase, its crystalline content and the degradation behavior of the Ca-P coating.

Sr.no	Name	Ca/P in terms of Atomic wgt (%)
1.	GH	1.77
2.	CGH	1.69
3.	rMGH	1.35
4.	rMCGH	1.67
5.	rTGH	2.31
6.	rTCGH	1.7

Table 4.9 Calcium to phosphate ratio was compared for GH and CGH, before and after seeding them with either rM and rT.

Work by K.R. Mohamed et.al. [239] also reported a decrease in Ca-P amounts in GH with Ca-P coating similar to the ones used in this study in comparison with rMGH, which is in accordance with the results obtained here with rMCGH. The effect of Ca-P coating on both rM and rT cell number was detectable for CGH scaffolds, and not for GH ones, which indicates physical presence of the Ca-P layer ('clogging' effect) had been of bigger importance that release of calcium and phosphate ions (chemical effect) [18]. rTGH with highest Ca/P showed a significant bioactive nature when compared with rTCGH. Therefore, rT cell proliferation promoted Ca-P depoition when seeded in CGH and rM responded in similar manner when seeded in GH was the the general conclusion drawn from the effect of cell-seeding on Ca/P.

4.2.6 Cytocompatibility

In vitro studies using the osteoblast have shown good biocompatibility and extensive osteoconductivity likewise from previous works [224]. The *in vitro* assays in **Figure 4.26** and **Figure 4.27**, were from cell co-culture studies done till culture day 28. Both rM and rT were seeded in the scaffolds and were cultured under condition physiological conditions with consistent change in conditioned media thrice a week.

DNA content along with cell viability and ALP activity with Ca^{2+} content was measured every week up-to culture day 28.

The maintenance of bioactivity during the fabrication step was proven in the mineralization step by ALP and ARS in the culture experiments with both the cell types in both the scaffold, in separate.

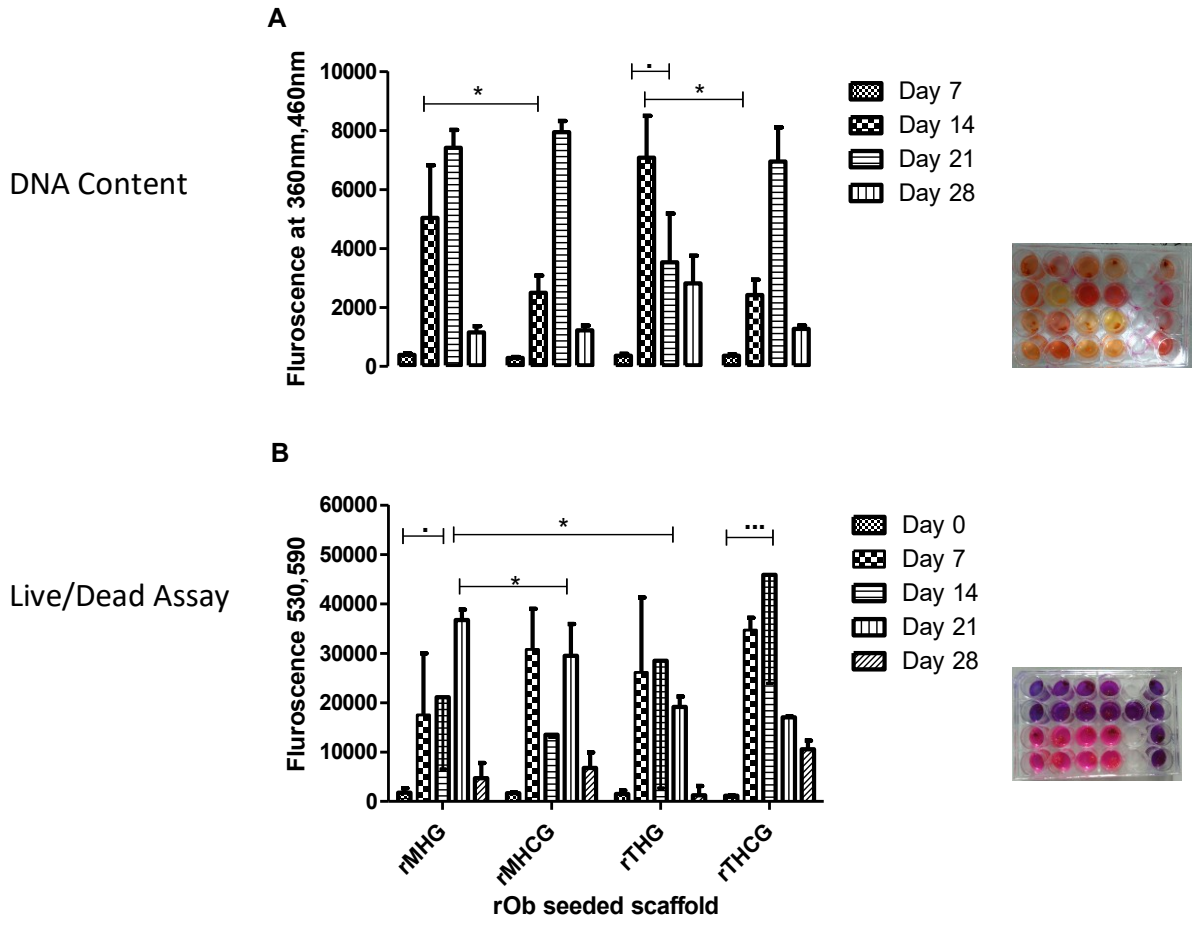

Figure 4.26 Relative expression (A)DNA content by the Hoechst 33258 (B) Growth kinetics via Cell viability and metabolic activity by AB assay in the four study groups namely rMGH, rMCGH, rTGH and rTCGH (n = 5).

4.2.6.1 Cell number

A possible reason for a significantly different trend of the DNA amount in rTGH was that the cells could optimally not use the complete scaffold for proliferation after day 14. This may be due to the contact inhibition, as no area was left to proliferate. For, rM in both GH and CGH, initiation of differentiation lead to decrease in the DNA amount. From the previous studies where tissue derived osteoblasts were cultured in GH to study the behavior of the primary cell line, a higher DNA concentration have been reported in the early culture days [240]. In this rabbit osteoblast based studies, the cell proliferation was influenced positively due to the presence of growth factors at early time point. This study combined that rT and rM showed significant difference in proliferation after culture day 4 and 7, respectively due to the presence of GH scaffold but no difference after culture day 28, which was due to saturation within the scaffold. The differentiation caused the decrease in the proliferation rate of rM on GH [92]. No significance difference was observed between the DNA amount of both the type of cell cultured in CGH over 28 culture days *in vitro* osteogenic culture. Whereas, the signicficance difference was noted between the type of cell seeded in GH, with rMGH showing the highest DNA amount among all the groups studied.

4.2.6.2 Cell Metabolism

Alamar Blue (AB) assay was done to study the metabolic activity of both the cells type when seeded in both the scaffold type. As seen in the **Figure 4.26**, the significant differences were observed between the cell type seeded on both the type of scaffolds in media over time.

Our *in vitro* results refer to the cell viability measurement which was essential in evaluating the capacity for the scaffold materials to support initial cell proliferation for new bone formation as per the most recent published work [116]. The proliferation of rOb

was determined quantitatively by ABA. Here period of 28 days of culture was associated with the growth curve of the synchronous cell population. Cell viability was assessed by AB assay after seeding equal concentration of cells in all the scaffolds starting on culture day 0 ($P<0.05$). From **Figure 4.26B**, rTCGH displays the highest significant viable cell population on day 14 followed by rTGH ($P<0.05$). rT unlike rM displayed parallel growth kinetics in the experimental groups [241]. This observation is also supported by FITC-**Cell cycle** analysis using the Flow cytometry displaying the overlap of rT and rM cell cycles shown in **Figure 4.18.** Also rMGH displayed significant variation w.r.t rTGH on day 21($P<0.01$) and w.r.t. rMCGH ($P<0.05$). After culture day 21, no significant variation was noted. Although in the calculation of cell metabolic activity in comparison to DNA concentration, discrimination exists with the progress in cell cycle over the culture days.

The quantification of osteogenic cells proliferation on these biomaterials done by ABA [181]. Isolated rabbit cells culture carried on each biomaterial at a concentration of $5X10^4$ cells/100µl up to culture day 28 day in the flat bottom 24-well cell culture plates. This culture duration associated with the growth kinetics of the synchronous cell population. **Figure 4.26B** indicates that each biomaterial promoted viability immediately after cell-seeding which significantly increased to 3 times the initial value over the culture duration. No significance difference was evident after culture day 21. Hence, all the biomaterials were cytocompatible but the cells seeded on CGH displayed ideal growth kinetics over the culture duration. Also, loss in CH biomaterial during sample aspiration for the assay resulted in the drop in metabolically active cell population around culture day 14. This loss then restored during the following culture day. Supposedly expected, our results suggest that >70% cells are viable on both experimental scaffolds groups for 21 days before the decline to depict death phase in culture (**Figure 4.26B**). AB assay allow to differentiates between the levels of metabolic activity of the cell population in

response to the type of biomaterial. These results were in agreement with the previous studies performed on polymer-protein-ceramic biomaterial [242].

4.2.7 Mineralization

4.2.7.1 Early mineralization marker

ALP activity defines the mineralization qualitatively after co-culture with the biomaterial as in **Figure 4.27A**. This assay revealved that the mineralization in CH is half of the value observed in CGH [101].This signifies the importance of gelatin as the organic matrix component for osteogenic cell mineralization [106]. ALP activity defined the progress in early-mineralization after rOb co-culture in the scaffold materials on culture day 7. The pattern of ALP activity of rT had no obvious differences when seeded in either GH and CGH. However, rTCGH displayed relatively higher osteogenic potential as CGH promoted early differentiaiton and stained in a dispersed manner than on GH. CGH when seeded with rT showed 1.25 fold rise in ALP activity after culture day 21. As expected ALP expression was found to continuously increase over initial culture time, with the siginificant difference observed on culture day 21. Both ALP activity and ARS mineralization determined the secreted and mineralized matrix cell's differentiation phase. ALP, an early marker of the ECM maturation during the differentiation of seeded osteoblast on the scaffolds is evaluated (**Figure 4.27A**). As observed that ALP activity increased distinctively after culture day 7 in all the scaffolds. Similar to the ALP activity trend, the osteoblast mineralization was reported to be the highest in rTCGH. In the seeded scaffolds, the osteoblast mineralization decreases following culture day 7. Maintenance of bioactivity in the scaffolds was proven in the culture experiments with rabbit osteoblasts of tissue origin.

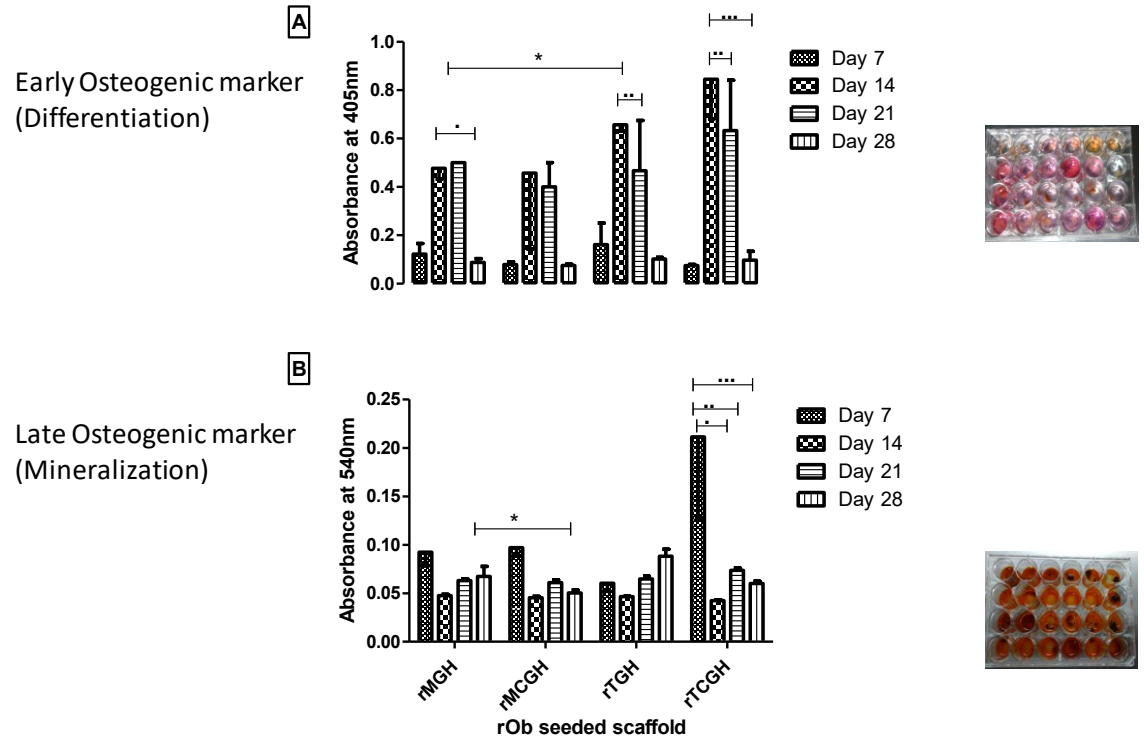

Figure 4.27 Relative expression of (A) Potency via Alkaline Phosphatase and (B) Calcium content by Alizarin Red S in the study groups namely rMGH, rMCGH, rTGH and rTCGH (n = 5), . All values are expressed as mean±S.D. · and * the indicates significant difference within group with P<0.05 and P<0.01 respectively.

4.2.7.2 Late mineralization marker

Initially high extracellular Ca^{2+} was observed due to inorganic-Ha component of the scaffold which successively dropped due to subsequent media washes before each absorbance reading. Post culture day 7, it was observed that Ca^{2+} deposition as matrix component was noted from ARS. The improved differentiation was parallel with the increase in the extracellular Ca^{2+} during mineralization [243].

It has been seen in **Figure 4.27B**, increase in mineralization is observed for all the scaffolds from culture day 7 to 14 then after drop in mineralization is noted for CGH scaffolds and only a slight rise for GH scaffolds irrespective of the type of cell seeded

[96]. The same being significant upon gelatin introduction as the organic matrix component. It affirmed the formation of the scaffold materials structure of ECM same as in the natural bone after differentiation.

4.2.8 Growth Factor gene expression analysis

The osteogenic nature of rT and rM in the *in vitro* scaffold samples is assessed from osteocalcin, collagen type I and BMP2 expression w.r.t GAPDH, the house keeping gene expression by real time PCR **in Figure 4.28**.

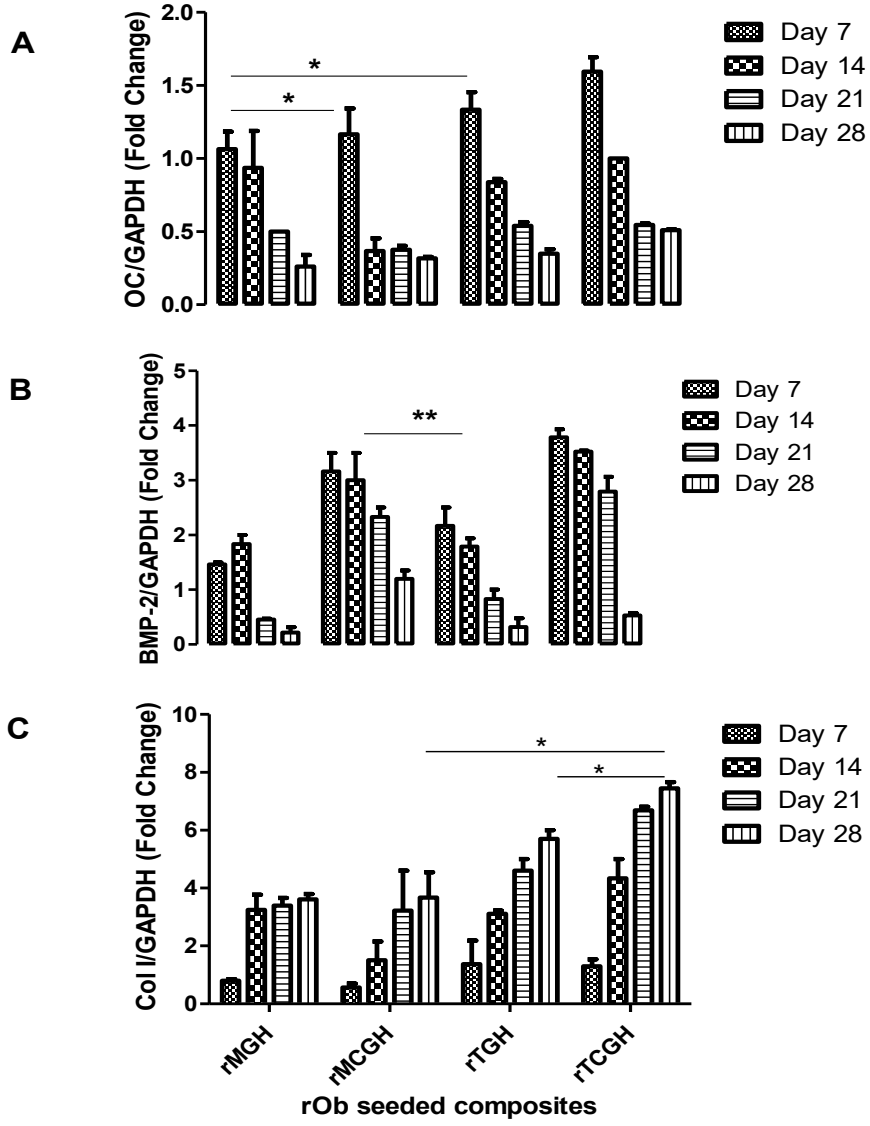

Figure 4.28 Relative expression of osteogenic growth factor genes: A. Osteocalcin, B. BMP-2 and C. Collagen I.

rT seeded scaffolds formed cellular aggregate from committed osteoprogenitor cell while rM seeded scaffolds form even cell clusters. BMP2 was the prominent regulator in driving differentiation of rabbit MSCs to pre-osteoblast [244].

With the progress in culture day each of the scaffolds shows an increasing trend in collagen type I gene expression while a decrease in expression is observed for both BMP-2 and osteocalcin as in **Figure 4.28** are also observed in [116]. Expression pattern of the individual gene w. r. t the housekeeping gene was also noted. Expression of OC via OC/GAPDH was parallel in all the cell-scaffold groups except rMGH, where the decline was uniform with the increase in culture day. In the rest cell-scaffold groups the decline in expression was non-uniform with being the most significant difference was observed between rMGH and rMCGH on early culture day 7. A 2-fold difference was clear between rMCGH and rTCGH also on culture day 7 for OC/GAPDH when compared within the cell-scaffold groups. Further, *in vitro* osteogenic differentiation of MSCs was promoted by the most potent BMP i.e, BMP-2 [213]. The effect of BMP-2 on OC was investigated, a significant decrease in OC expession with increase in BMP-2 was found in case of CGH based cell-scaffold groups only [6]. BMP-2/GAPDH expression results revealed lower BMP-2 expression in GH cell-scaffold groups compared to CGH groups [17,92]. The expression of col I increased over time from culture day 7 to 28. This increase was linear over time in CGH groups, but sudden in GH groups post culture day 14. This supported osteogenic induction in all the cell-seeded groups under investigation [245]. Thus, the effect of BMP-2 on col I expression was related inversely following both osteogenic differentiation and induction in rM and rT, respectively. As BMP-2 binds to the DNA sequences specific for transcription which were involved in osteospecific differentiation [23,240]. *In vitro* BMP-2 directed the deposition of both collagenous and non-collagenous matrix protein. Moreover, **Figure 4.28B** results display that chitosan

enhanced the osteoblastic differentiation of the MSCs since the BMP-2/GAPDH expression for CGH scaffold is significantly higher immaterial of the cell-type seeded in the scaffold. **Figure 4.28** shows that over the 28 day culture period, rT when seeded on the scaffolds expressed marginally higher levels of both OC and col I than those by the rM population. The gene expression profiles suggested that BMP-2 played supportive role in osteoblast maturation for ECM production. BMP2 level of expression in cacified CGH composite, was the highest on culture day 7 and then decreased by day 21 as osteogenesis became prominent, favoured the use of CGH composite when seeded with rT.

On culture day 7, significantly the highest level of expression of OC(1.5 fold) on CGH composite than GH (**Figure 4.28A**), a decrease in BMP2 (2 fold) expression on calcified CGH on day 14 (**Figure 4.28 B**) is seen with no significant difference at this point. With drop in abundant calcium binding protein, mild drop in adsorbed Ca/P was observed with decrease in OC. CGH facilitated increase in calcium deposition nucleation sites and growth over the scaffold structure leading to the activation of osteoblast receptor which resulted in higher levels of OC expression in rT-seeded scaffold.

4.2.9 Growth factor expression

The protein expression pattern was validated by running the immunoblot for the isolated protein samples from the respective osteoblast seeded-scaffold group on culture day 21.

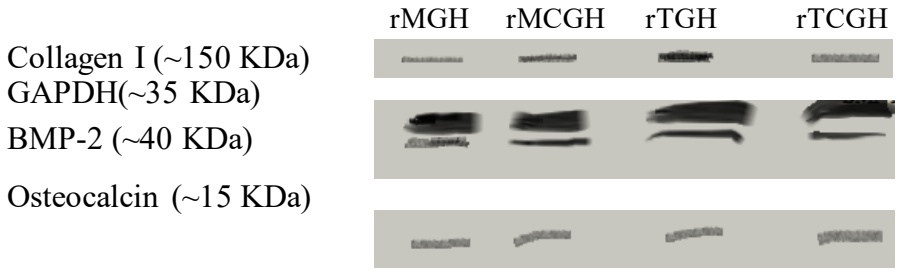

Figure 4.29 Immunoblot of Collagen I, GAPDH, BMP-2 and Osteocalcin in the cell seeded scaffolds: rMGH, rMCGH, rTGH and rTCGH.

Independent blots are displayed together in **Figure 4.29**. Distinct broad bands were observed for the house keeping gene, GAPDH. The immunoblot results were supportive of the the PCR results.

4.2.10 Biochemical Analysis

Mineralization mainly due to type I collagen were observed at collagen concentration of 0.11 µg/100 µl HCl for rTCGH. Non-protein matrix component, Osteocalcin concentration was 0.00126µg/ µl DPBS on culture day 7 for rTCGH.

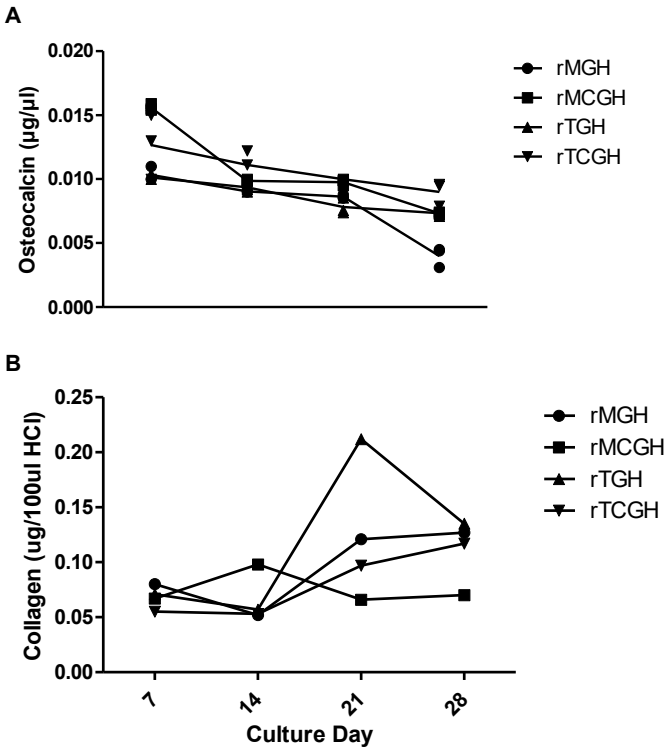

,

Figure 4.30 Collagen I and osteocalcin expression analysis in the rabbit osteoblast cell seeded scaffolds: rMGH, rMCGH, rTGH and rTCGH.

4.2.12 XRD analysis

From the synthesised Ha, the existence of peaks at approximately 22, 26, 29 and 32°, corresponds to the diffraction planes at (211), (002), (210) and (300) respectively, confirmed the formation and exitence of Ha in the synthesised scaffold materials. These peaks refer to the rMGH, rMCGH, rTGH and rTCGH respectively. Crystallization in the synthesised scaffold materials, indicated the existence of inorganic part, meanwhile decrease in intensity is shown in **Figure 4.31** indicating resultant interfacial bonding between the particles and matrix.

The XRD patterns of both the cell types seeded in GH and CGH, respectively were compared in **Figure 4.31A-B**. The incorporation of gelatin into the chitosan and Ha was evident by the XRD data of GH and CGH. The chitosan peak (2θ=20.02) was distinctively evident in all four groups and has shown increased intensity in CGH when seeded with rT over rM. Both the scaffolds were shown to be crystalline, with the relative crystal content of CGH was more than in GH both before and after seeding with either rM or rT. Peak values for the osteoblast-scaffolds are summarised in **Table 4.10.**

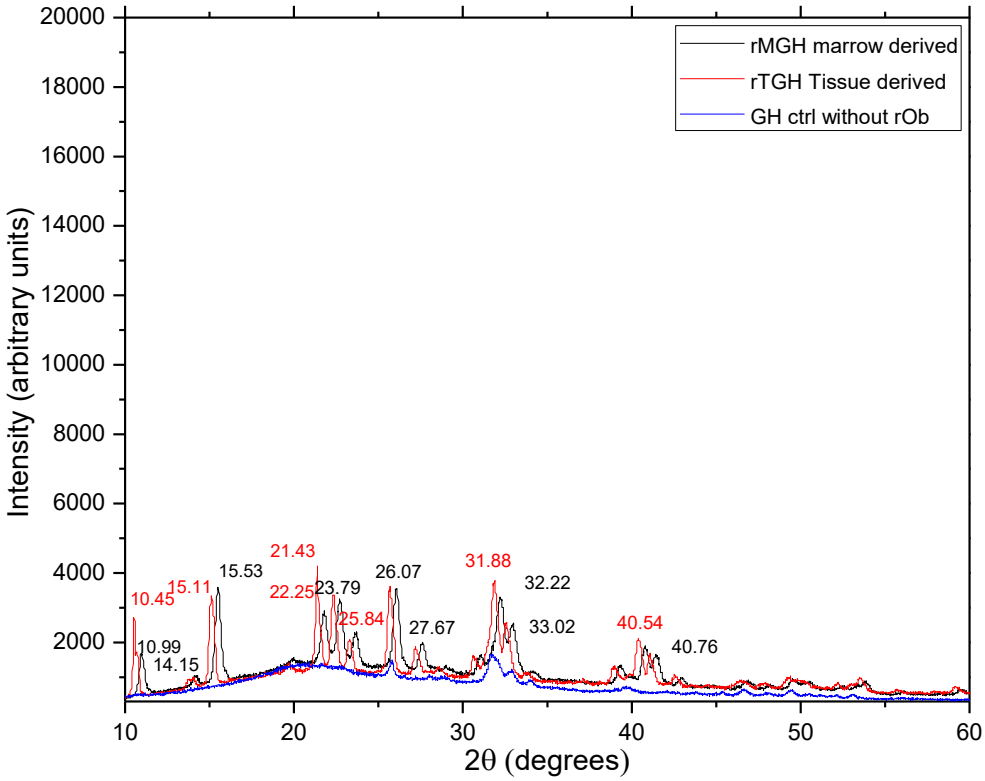
rMGH marrow derived
rTGH Tissue derived
GH ctrl without rOb
Intensity (arbitrary units)
2θ (degrees)
10.45
15.11
15.53
21.43
22.25
23.79
25.84
26.07
27.67
31.88
32.22
33.02
40.54
40.76
10.99
14.15

A.

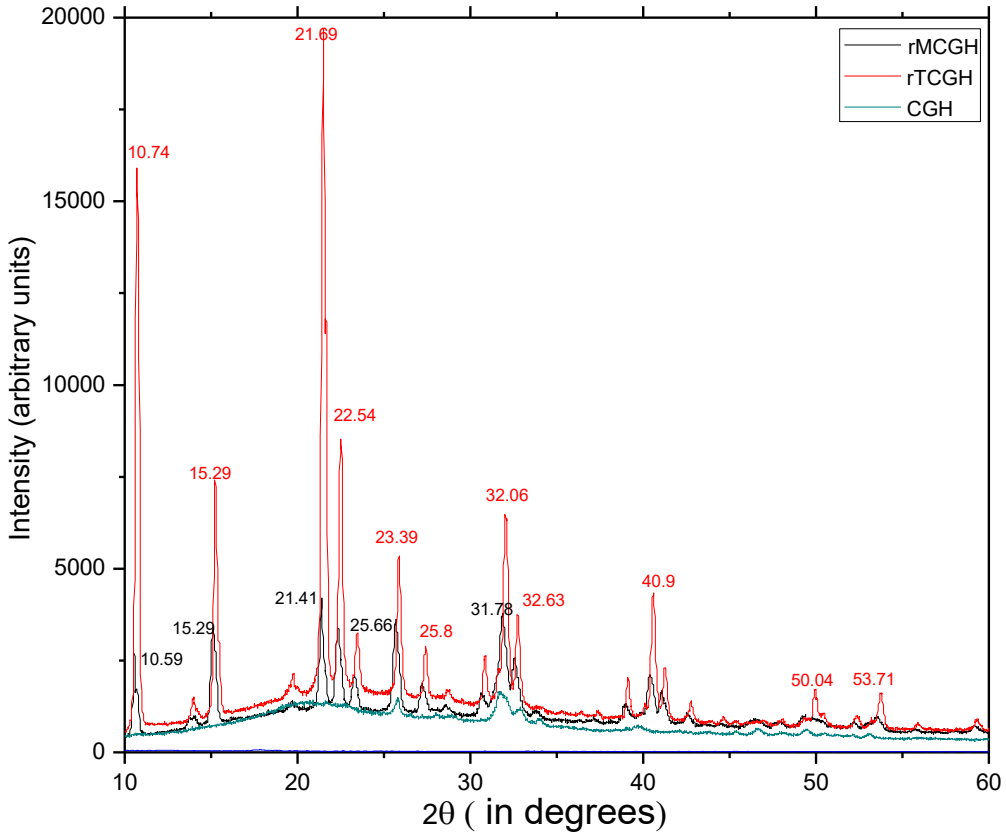
rMCGH
rTCGH
CGH
Intensity (arbitrary units)
2θ (in degrees)
10.74
21.69
22.54
15.29
32.06
23.39
40.9
21.41
15.29
25.66
31.78
32.63
25.8
10.59
50.04
53.71

B.

Figure 4.31 Crystallinity pattern of the the rabbit osteoblast cell seeded scaffolds: A. rMGH and rTGH and B. rMCGH and rTCGH from XRD.

Sr. No.	Cell-Scaffold material	2θ (in degrees)	Peak specificity
1.	rMGH	10.5, 15.57	
2.	rMCGH	10.42, 22.15 31.7	 Ha
3.	rTGH	10.59, 15.29, 21.41	
4.	rTCGH	10.74 21.7	 Chitosan and gelatin [224].

Table 4.10 Peak specificity in the the rabbit osteoblast cell seeded scaffolds: rMGH, rMCGH, rTGH and rTCGH.

4.2.13 FTIR analysis

FTIR spectra was recorded for all scaffold samples after seeding them with rabbit bone cells are presented in **Figure 4.32**. The characteristic peptide bonds band can be seen in the FTIR spectra of both rMCGH and rTCGH.

The FTIR analysis indicated the presence of chitosan bands in the scaffold also after mineralization was established by the seeded osteoblast [246]. Natural bone hydroxyapatite ftir peaks were distinctively retained after cell seeding [209]**.**

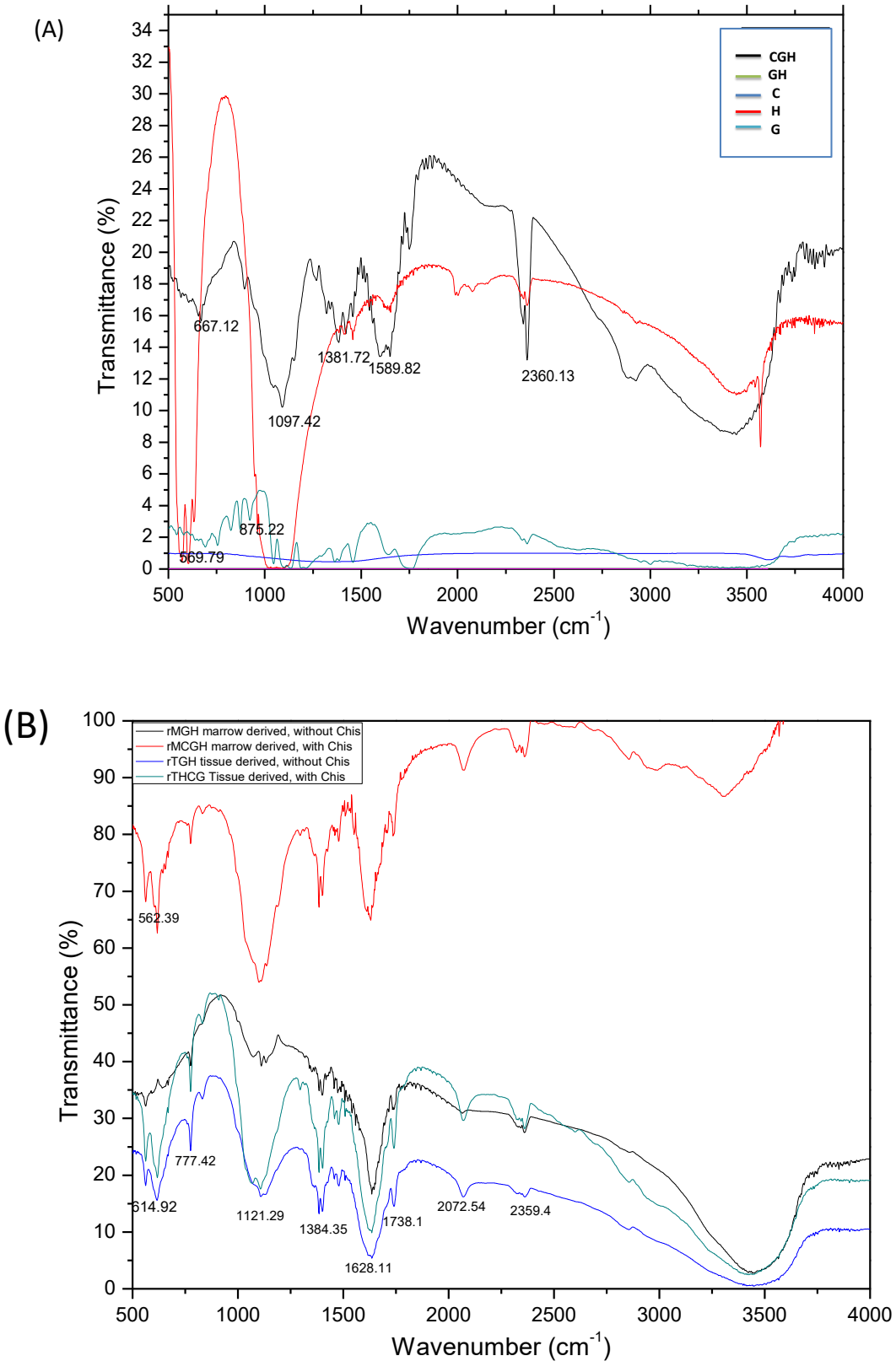

Figure 4.32 Transmittance intensities of the scaffolds after seeding them with either rM or rT namely rMGH, rMCGH, rTGH and rTCGH.

Intensity / Groups	PO_4^{3-}	O=C-N		$*PO_2^-$	C=O COO^-	H-O-H bend	C=O amideI	-C=O		O-H in -COOH
	557	614	777	1121	1384	1628	1738	2072	2369	3469
#1 rCH	+	+	+	+	+	-	-	-	+	-
#2 rCG	-	+	-	+	-	-	-	-	-	-
#3 rGH	+	+	+	+	+	+	+	+	-	+
#4 rCGH	+	+	+	+	+	+	+	+	-	+

*Symmetric stretch [31]
**Asymmetric stretch

Table 4.11 FTIR derived strengths and the assigned groups are displayed for the cell seeded scaffold materials.

Intensities present at 777cm^{-1} and 1384 cm^{-1} were related to the presence of CO_3^{2-}. After the most accurate identification, the bands at 562 and 61 cm^{-1} corresponded to PO_4^{3-}. 1121 cm^{-1} were clearly detected in crystalline Ha: $Ca_{10}(PO_4)_6(OH)_2$ [204].

When the *in vitro* studies were carried out with rabbit osteoblast seeded on selected GH and CGH regardless of the medium (growth or osteogenic), rT were able to adhere and proliferate within both the scaffolds,. However, improvement in proliferation was noticed after the introduction of the osteogenic media (by nearly 1.5 fold in 28 days) in the classical tissue culture plate. In addition, rM were able to proliferate when supplemented with the osteogenic factors as observed from the marker gene expression data. Maximum proliferation and mineralization potential have been observed for rT seeded and cultured in CGH from the *in vitro* cell studies in both the type of scaffold materials, GH and CGH. While developing the suitable scaffold for bone regenerative studies, CGH was found to retain the surface and 3D-core morphology post seeding and subsequent culture in with rT.

4.3 Human osteoblast-based studies

4.3.*1 in vitro osteoblast* attachment, proliferation and morphology

Hoechst33258-nuclear staining of live cells and alexa flour 488-cytoskeleton staining was done after day 14 in culture to determine cell attachment behaviour of the hMGH, hMCGH, hTGH and hTCGH scaffolds. The cell proliferation was also observed in the cell-seeded composite by CLSM (**Figure 4.33**). Bone cell seeded on hMCGH and hTCGH showed well-spread morphology unlike on hMGH and hMCGH. The CLSM results showed that in bone cell were partly-attached to the composites and have round shape in hMCGH and hTCGH.

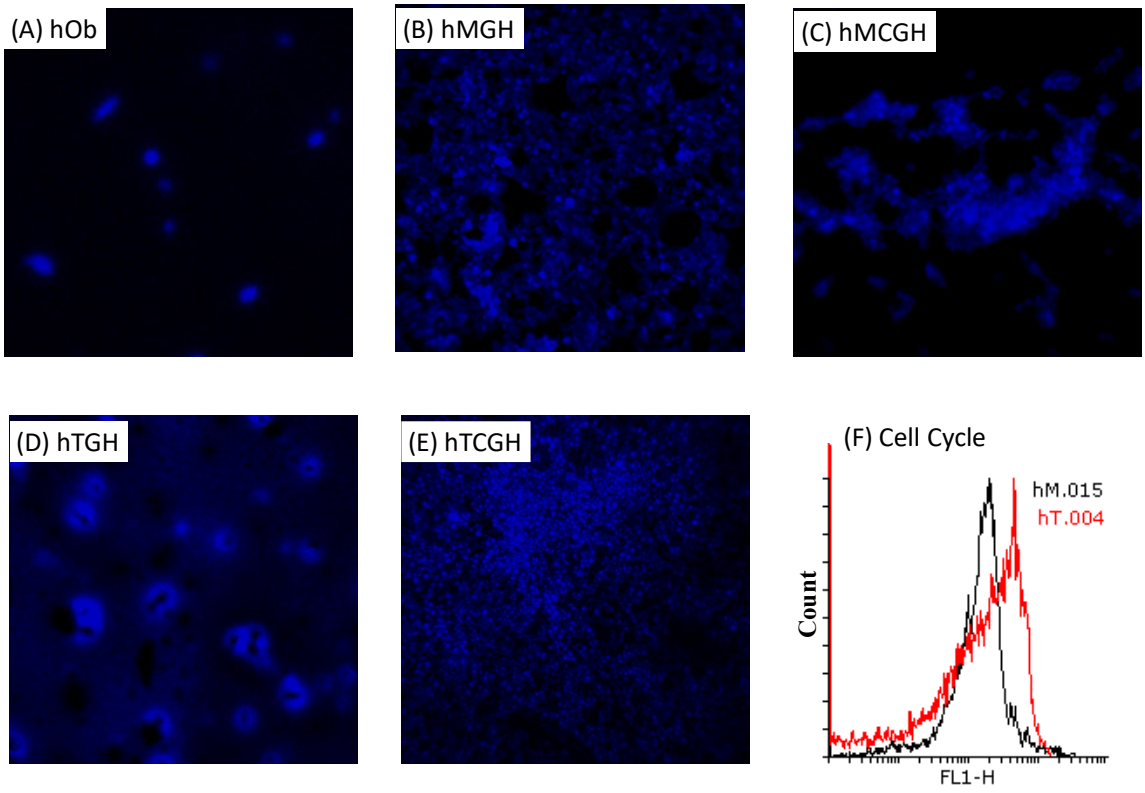

Figure 4.33 Fluorescence micrographs of human Osteoblast cultured in the scaffolds (B-E) FACS analysis of (A-E) CLSM Hoechst 33258 labelled nuclei in the osteoblast seeded composites and (F) Human osteoblast cell cycle analysis.

In all four of the scaffolds, the cells were attached completely, displaying branched morphology and hence nontoxicity of composite [55,111]. From the cell cycle analyzed, the percentage of cells in the G_0/G_1, S and G_2/M phase and determined by alexa flour 488-FACS on bone cell groups is shown in **Figure 4.34**. hT showed the higher proliferative population in S phase compared to hM when the unstained population was used as a control also observed by C.Gandhimati et.al. [247]. From the CLSM and flow cytometry data, hMCGH and hTCGH were selected for further studies.

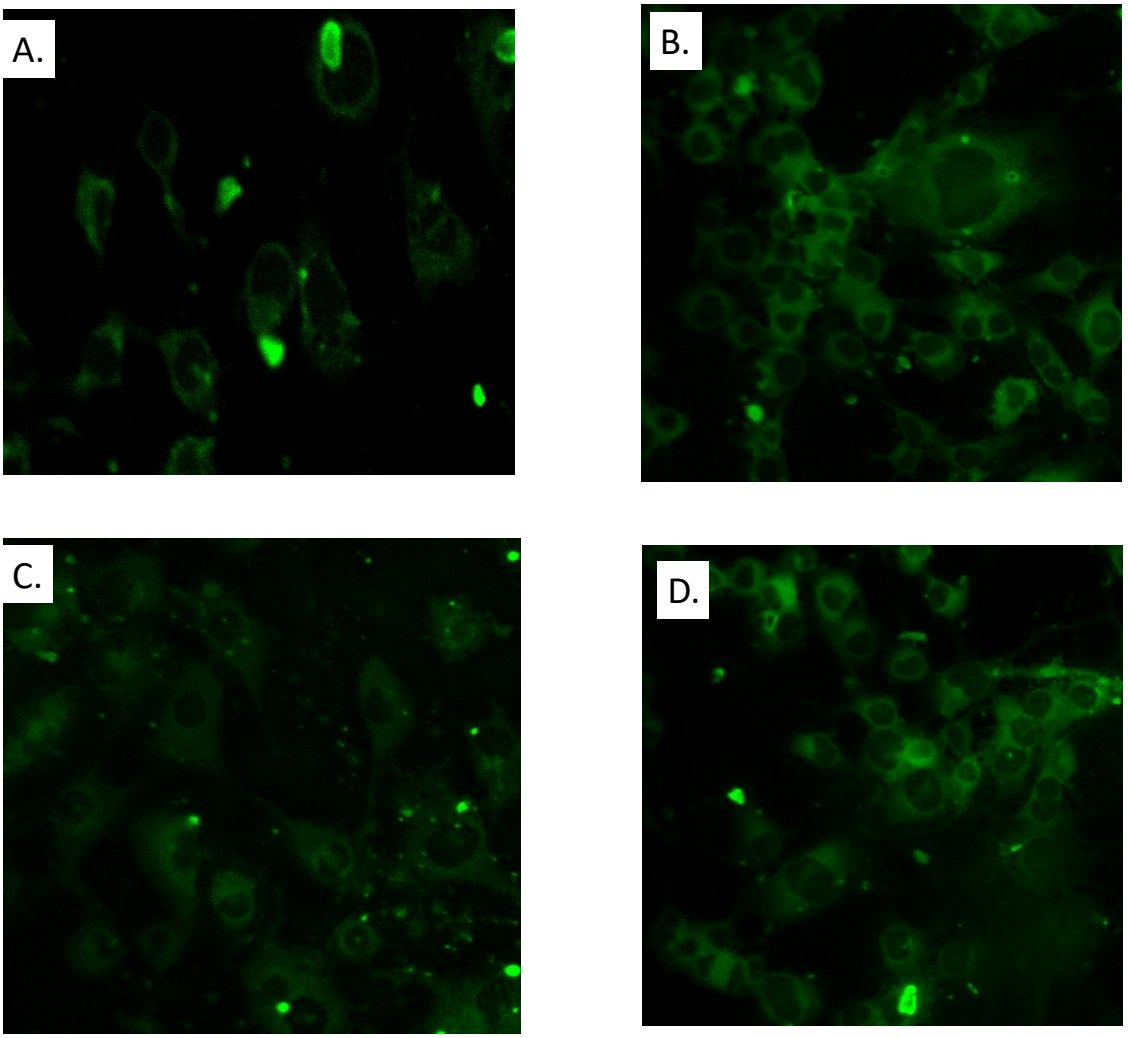

Figure 4.34 Fluorescence micrographs of Alexa flour 488 labelled 'human Osteoblast cultured in the scaffolds' (A) hMGH, (B) hMCGH (C) hTGH and (D) hTCGH (Magnification-63X).

4.3.2 Morphology analysis

Figures 4.35 showing the cell spreading and mineralization of hT in CGH with arrows pointing to the crystal deposits. It was observed that human cell adhesion improed by Ha [248], as there is calcium phosphate mineral deposition. The cell-scaffold conjugate were evaluated and results were shown herewith.

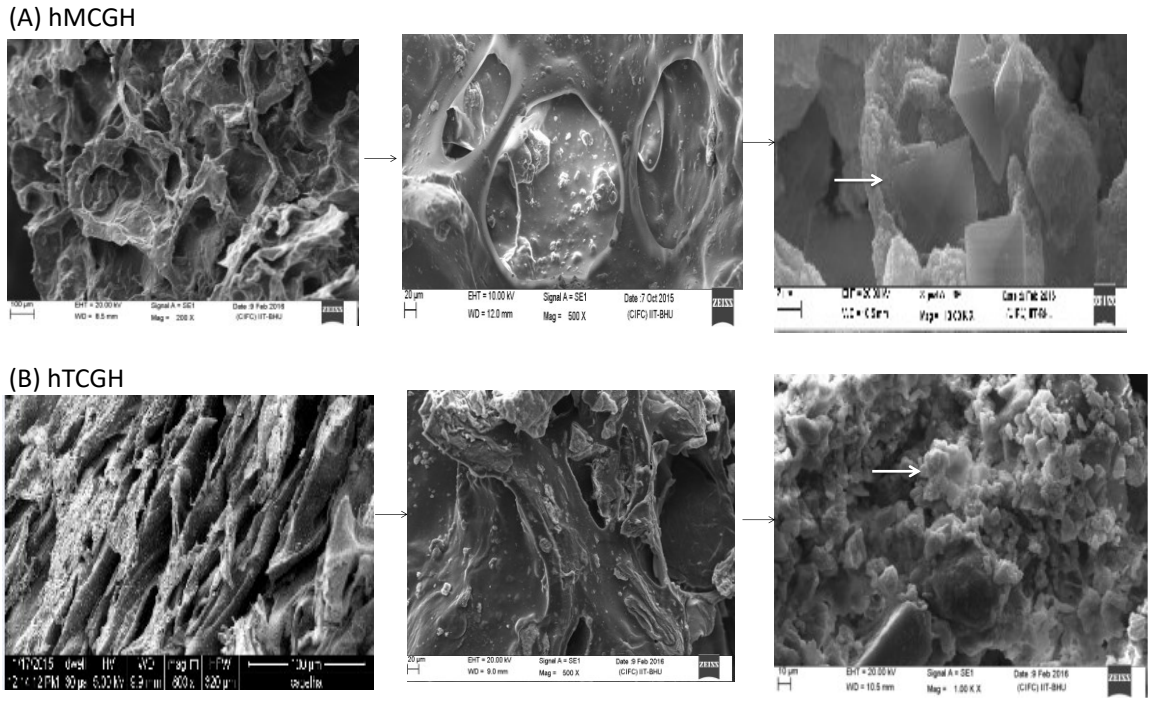

Figure 4.35 SEM compares the pore morphology and mineral deposition in the CGH scaffolds (A) hMCGH and (B) hTCGH.**Arrows show the cells that have adhered to the scaffolds.*

4.3.3 Thermal behaviour

DSC was done to evaluate the thermal behavior of human bone cell seeded-composite. The fraction of Ha determined the degree of crystalline behaviour in the composites [249]. From DSC thermograms shown in **Figure 4.36**, the intensity of the exothermic peak increased with Ha inclusion as the composite component. Also, the recrystallization

phenomenon was distinctly visible in rTCGH but become negligible in the other seeded scaffolds.

Figure 4.36 shows that the endothermic effect among the composites after 200 °C was associated with the melting temperature of gelatin.

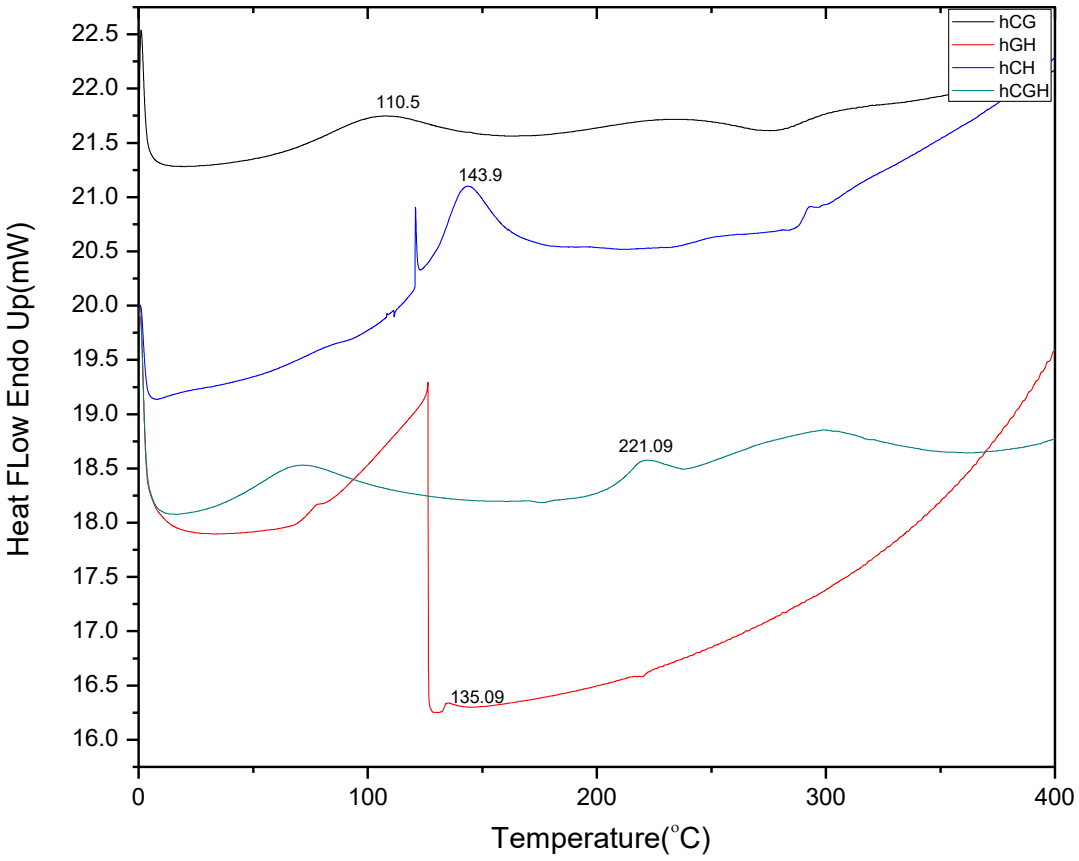

Figure 4.36 Thermal behavior of human cell seeded scaffolds with indicated T_g value: A. hMGH, B. hMCGH, C. hTGH and D. hTCGH (with T_g value indicated).

In addition, along the same curve, characteristic peak of Ha were observed.

The cold crystallization temperature (T_{cc}) of CG biomaterial composite increased initially. Ha inclusion promoted drop in T_{cc} with increase in its concentration in the composite due to decrease in contact within the gelatin based matrix. Also, multiple melt peaks were observed in hMCGH decreased to distinct two peaks after bone cell seeding.The Tg in

hMGH being the lowest, likely because of the size, Ha crystal phase was consistently reduced but later strengthened because of the cell-matrix interactions after cell seeding. This indicates that Ha could act as the nucleation site for crystallization in the composite, whereas in GH with no chitosan resulted in slower decomposition with the pattern being distinct than the other composites in the study group [250][92].

4.3.4 Chemical Analysis

4.3.4.1 XRD analysis

SEM and XRD investigated bone cell deposited Extracellular matrix calcium-phosphate (Ca-P) crystals at the micro and macroscopic level respectively. In accordance, XRD plotted in **Figure 4.37** shows that the primary phase was Ha based.

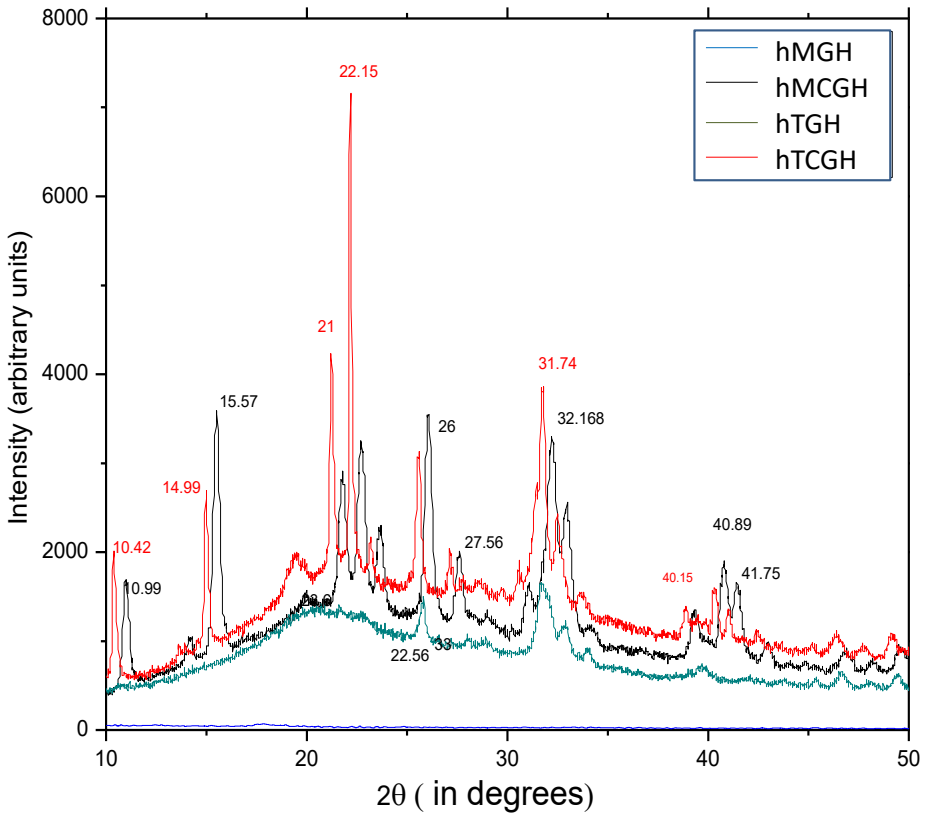

Figure 4.37 XRD demonstrating quantitative phase development in the scaffold after seeding with either osteoblast of human origin (rM or rT) A. hMGH, B. hMCGH, C. hTGH and D. hTCGH.

These results confirmed that the GH and CGH had bioactivity and might be positive in replacing natural human bone. The XRD results of the bone cell loaded composite in **Figure 4.37** displayed peaks none observed before bone cell seeding. Peaks associated with the crystalline inorganic Ha were prominently detected. Their relative intensity rose enormously in CGH in comparison to GH in synchronisation with EDX Ca/P ratio (**Table 4.2**). From **Figure 4.37A**, CH has inherited maximum crystalline behavior among all the composites followed by CGH. CH exceeded in being brittle with increase in crystallinity exceeding the threshold value for natural human bone. After composite fabrication in GH, the crystallite inorganic Ha role decreased in the composite, meanwhile increased post-seeding as shown in **Figure 4.37B**. The characteristic Ha peaks were present but not altered significantly among groups studied, result from inorganic phase development around gelatin matrix. The arbitrary units (a.u.) in bone cell seeded CH and CGH became sharper and stronger in intensity in comparison to CG and GH. The shift, decrease in intensity, and missing intensities (e.g., $2\theta=40°$ in CH peaks were narrower and prominent than in CGH) of the consecutive peak of the composite and hinted towards bonding between gelatin matrix, Ha, and chitosan. It showed chitosan's role in increasing bonding peak intensities nearly by five times, by bonding with Ha in Gel matrix.

4.3.4.2 FTIR analysis

FTIR interpretation confirmed the crystalline percentage and physicochemical properties which enable peak shifting indicating molecular interaction. FTIR of cells was done to know the mineral phase constitution deposited by cells upon co-culture. As the functionally active group engaged in bond formation, for the cell-seeded composite the increase in peak intensities was observed unlike primarily decrease transmittance in the composite without cells **Figure 4.38**.

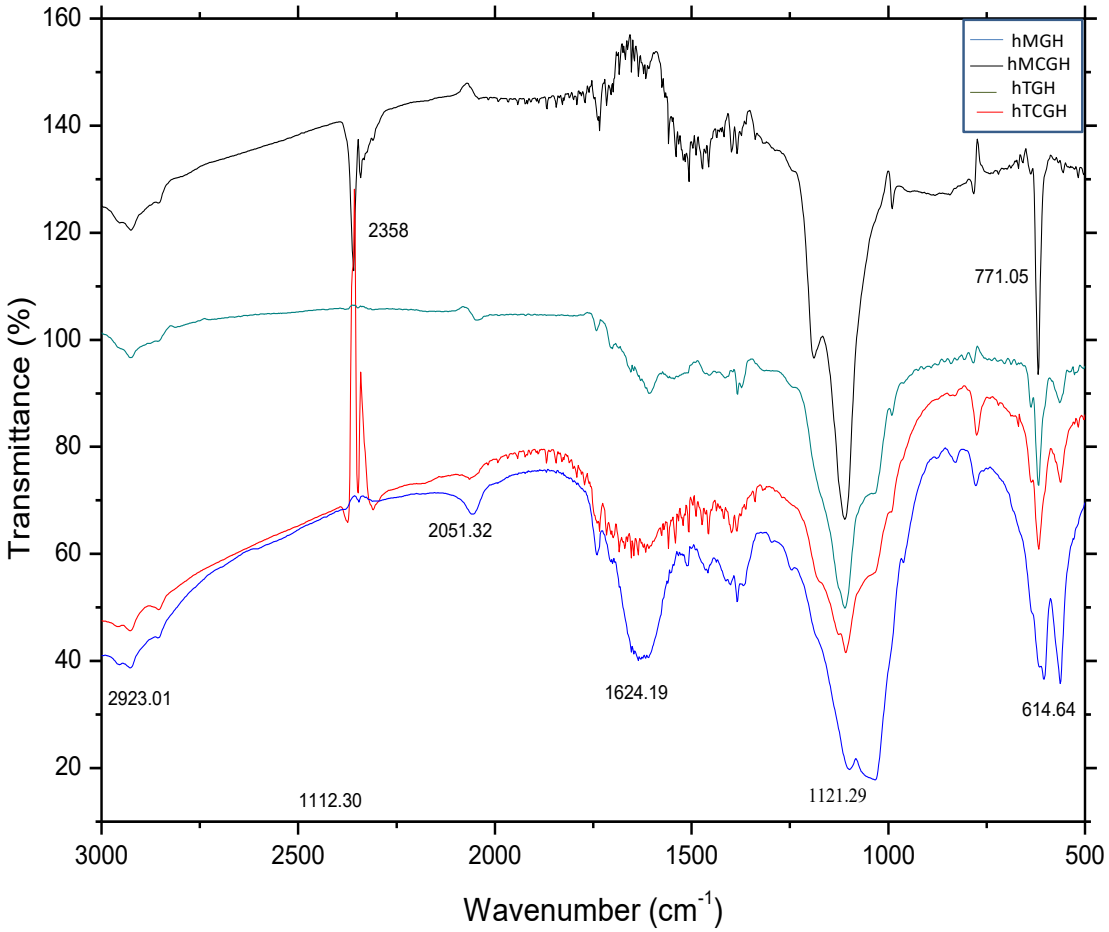

Figure 4.38 Quantitative FTIR spectra of scaffold after seeding and culturing with osteoblast from human namely: hMGH, hMCGH, hTGH and hTCGH.

FTIR data revealed the critical information about interactions between the Ha-based dispersed inorganic phase and the Gelatin-based matrix both with and without human osteoblast seeding.

These composites demonstrated overlapping FTIR characteristic peaks but with peak shift and the difference in peak intensity, presented in **Figure 4.38**.

Distinct bands were observed for the cell-seeded composites. The sharp peak at 614 corresponded to phosphate group stretch vibration after ECM coating. The strong peak at 771 was related to Amide IV mainly 0=C-N deformation. The sharp peak at 1112 was related to ester C-O asymmetric stretch. Meanwhile, hCH showed the only prominent peak at 1624(variable intensity C=C stretch, Amide I, II, III) unlike the other 3 in the cell-

seeded group. Crystalline hydroxyapatiite contained carbonate ions at 1624cm^{-1}. The peak at 2051 corresponds to C=O stretch, the peak at 2358 was also reported in high-temperature extracted gelatin which displayed distinct amide III peaks like bone gelatin [238]. The medium peak at 2923 is for C-H stretch.

However, there was a significant difference between the spectra: the characteristic peak of carbonate group at 771 cm^{-1} nearly disappeared in the hCGH (**Figure 4.38**). In contrast, the CG based matrix showed higher intensity w.r.t. the rest of the composites at 1121.29 which indicated a strong vibration due to C-O and C-N stretch. This bond may be indicative of active bonding between calcium ions and carbonyl (C-O) bonds.

Peak shift observed from 1930-2070 corresponds to C=N stretching vibration from the formation of water-nitrile complexes. This exciting phenomenon strongly favoured the configuration of GH and CGH. In the absence of hydrophilic chitosan, the fingerprint region showed shallow peaks. More groups in the Gelatin-based matrix begin to assemble with chitosan addition [122].

4.3.5 Cytocompatibility

4.3.5.1 Metabolic behaviour of human osteoblast

The DNA concentration and the Metabolic behaviour of human osteoblast was also studied as that of the rabbit osteoblast, using Hoechst 33258 and fluoremetric alamar blue assay. Parallel results were observed with significantly higher concentration DNA and viable population in case of hTCGH. However, the hMCGH scaffold displayed least viable populated unlike rMCGH (**Figure 4.26**).

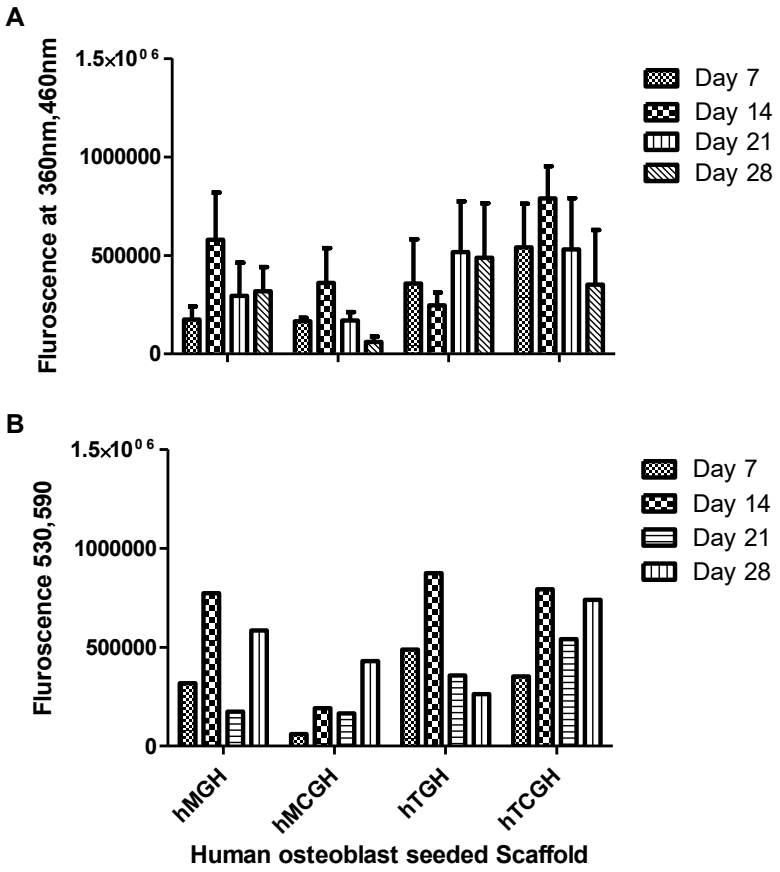

Figure 4.39 Fluorescence measure of the A. DNA concentration and B. Metabolic activity of the four groups of cell-seeded scaffolds (hMGH, hMCGH, hTGH and hTCGH).

4.3.6 Mineralization

Early mineralization was found for hM seeded scaffolds in comparison to the hT seeded scaffolds. Howerver, mineralization lasted longer and at higher rate in hMCGH and not hTCGH.

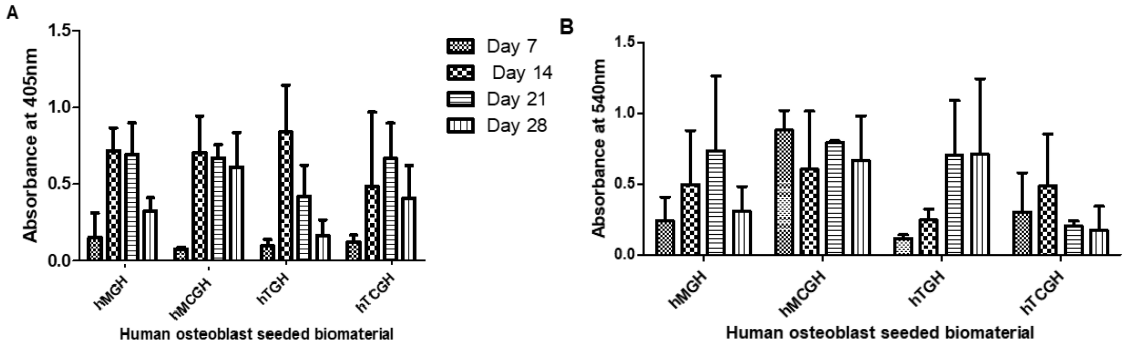

Figure 4.40 *In vitro* studies of the four groups of cell-seeded scaffolds (hMGH, hMCGH, hTGH and hTCGH) to determine A. Early marker of differentiation B. Late marker for mineralization from ALP activity and calcium deposition from Alizarin Red S (ARS), respectively.

4.3.7 Biochemical analysis

4.3.7.1 Collagen and osteocalcin

Mineralization mainly due to type I collagen was also observed at collagen concentration of 2.231 µg/100 µl HCl for hTCGH. Non-protein matrix component, Osteocalcin concentration was 0.0016µg/ µl DPBS on culture day 7 for hTCGH.

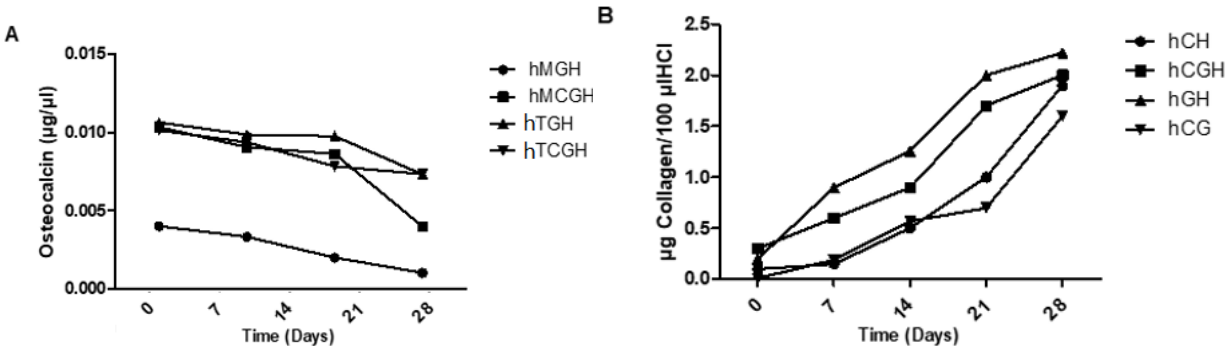

Figure 4.41 Biochemical markers of mineralization A. Collagen I and B. Osteocalcin.

4.3.7.2 Determination of the Glucose Diffusion Coefficient (D)

The varying surface and core morphology tend to influence the diffusion of the glucose moieties. Hence, the value of D is directly correlated to both, the porosity and morphology.

Figure illustrates the changes in glucose concentration over a period of eight hours from 0 to 27 culture days.

The GH based scaffold depicts lesser degree of diffusion than the CGH scaffold. Also, rTCGH displayed maximum glucose diffusion, independent to its rate of biodegradation.

Also, the hT seeded groups (hTGH and hTCGH) displayed marginally lower resistance to glucose diffusion over the hM seeded groups (hMGH and hMCGH).

The effective glucose diffusion coefficient was higher for CGH groups than the GH groups.

From the study done by H.Suhaimi et.al. the diffusion coefficient for the scaffold material increases at 37ºC.

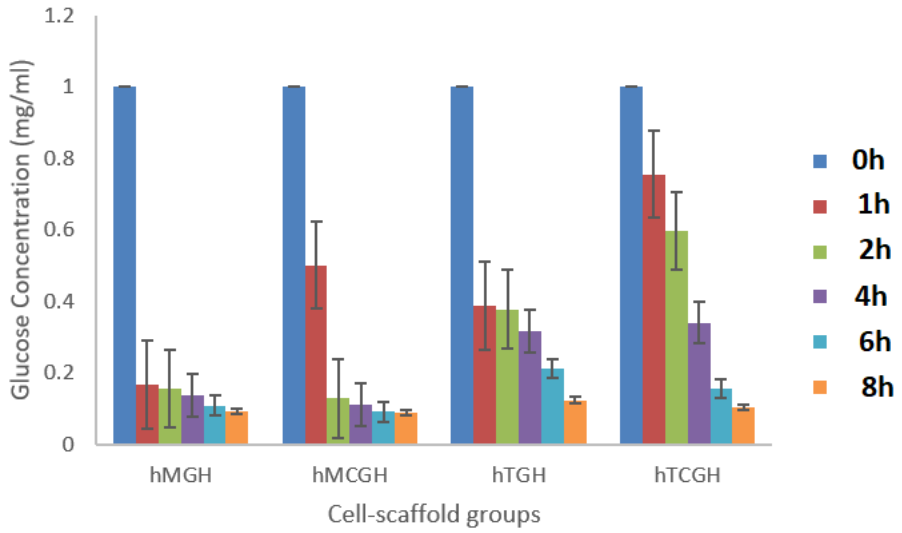

Figure 4.42 Variation in the glucose concentration w.r.t time factor among the four cell-scaffold groups: hMGH, hMCGH, hTGH and hTCGH

Sr. no.	Cell-scaffold group	Std Deviation (σ)	D (m^2/s) After 27 culture days
1.	hMGH	2 ±2.67* 10^{-10}	2.05±0.77* 10^{-10}
2.	hMCGH	2.05±0.11* 10^{-11}	1.05±0.1* 10^{-11}
3.	hTGH	NA	1.011±2.66* 10^{-10}
4.	hTCGH	9.01±0.66* 10^{-9}	7.05±0.12* 10^{-9}

Table 4.12 Effective diffusion coefficient with standard deviation for glucose across cell-scaffold saturated with cell culture media.

4.4 *In vivo* evaluation of the scaffold rTCGH

4.4.1 Clinical observation after rTCGH implantation

'rT cells loaded in cylindrical CGH' and implanted in the same white rabbit wherein surgically the 'critical-defect site' was created. Surgical implantation of the scaffold was done successfully using the press-fit technique and blood was seen to fill the implantation site. All the animals recovered well post-operation and ambulated freely within 7 days, with no signs of limping or distress till the duration of the study. No post-operative complications were seen up to the 12 weeks' time point.

4.4.2 Macroscopic assessment of the bone defect repair

The gross visual macroscopic evaluation of the defect in a load-bearing tissue to be repaired was carried out at the defect opening.

At the time points of scaffold retrieval, no evidence of degeneration, migration, delamination of the construct or inflammation was seen. The scaffold demonstrated successful site-fixture after 2 weeks into implantation mimicking the natural-repair of the bone defect. After 4 weeks, defect-site displayed signs of healing in terms of defect-closure efficiency to ~30%. By the 8th week, good level of filling was observed with signs of integration with the neighbouring healthy tissue. The 'control defect-site' showed

limited tissue-integration resulting in the incomplete defect-fill. The healing was restricted to the edges up to ~30 days.

With the progress into the 12th week of implantation, improved tissue regeneration with noticeable fissures as close to the surrounding native tissue were seen. However, both the control and implanted site initially displayed visible signs of depressions and tissue breakage, respectively.

The CGH scaffold after implantation displayed no clinical evidence of inflammation or host cell response to the foreign body *in vivo* for upto 12 weeks also observed by H.Jin et al [251]. Hence, CGH was found to be biocompatible *in vivo*. The *in vivo* optimal conditions were different from the *in vitro* set parameters, the degradation behaviour was different too. In the in vitro degradation study, it took >28 days for the scaffold to degrade completely whereas *in vivo* the scaffold degraded by the 12th week.

In spite of the post-implantation duration, atypical foreign body in response to the presence of scaffold was not found in newly synthetized tissue located in the area all around rTCGH.

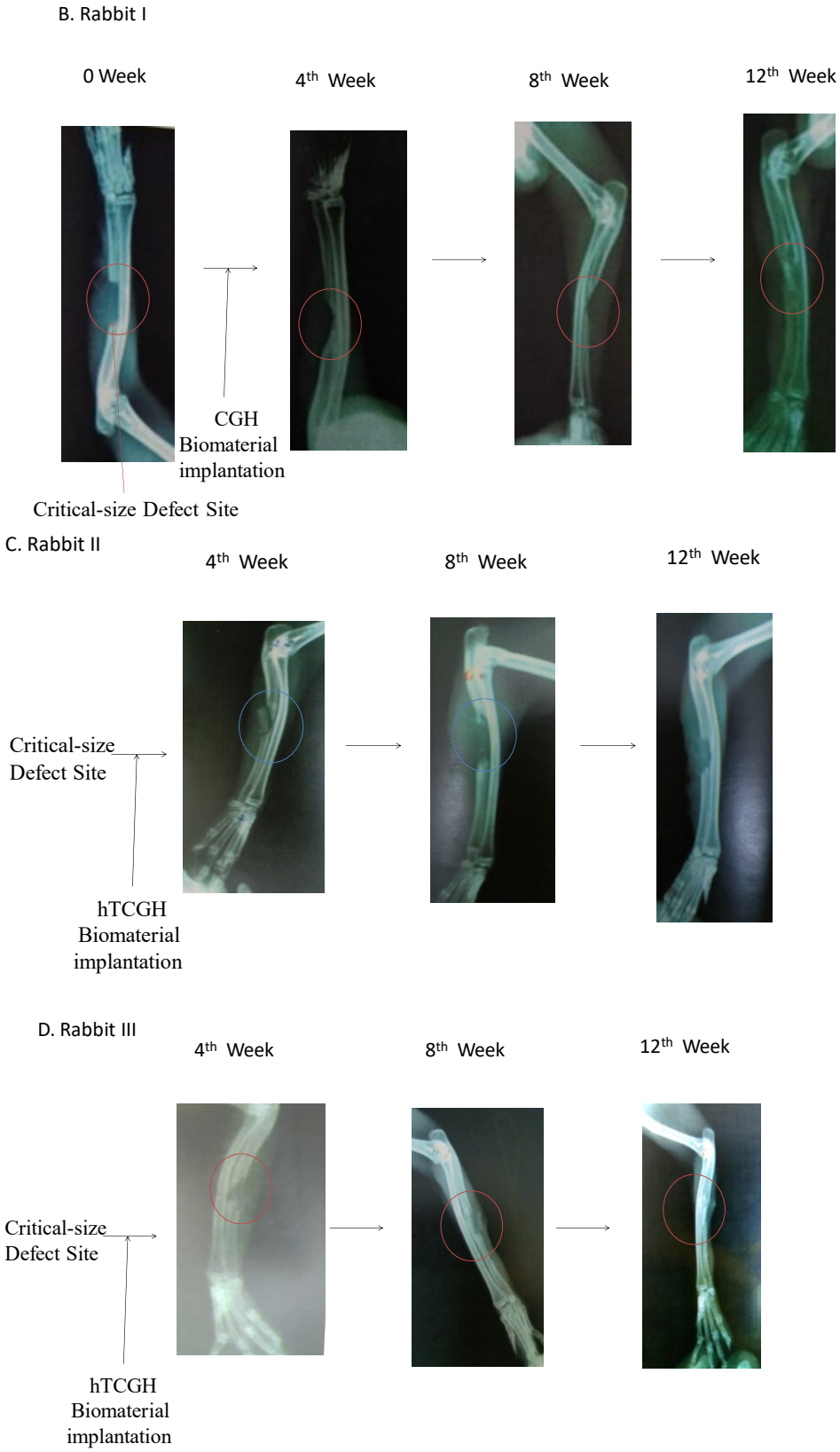

Figure 4.43 Progressive *in vivo* display of the rTCGH scaffold implantation at the critical-defect site in the rabbit ulna (X-ray images)

In the parallel lines with the observations recorded from the *in vitro* studies, the improved bone regeneration can be seen *in vivo.* It can be explained from the increased recruitment of the endogenous osteoblastic lineage from the microenvironment of the defect site, along with the proliferation of rT throughout the rTCGH scaffold. The geometry of rTCGH scaffold border allow it to fit in the defect-site establishing intimate contact due to the scaffold elasticity (**Figure 4.42B-D**). The density after bone mineralization on the scaffold-defect border increased throughout the 12 weeks of implantation for the rabbits implanted with the rTCGH scaffold (**Figure 4.42**). **Table 4.12** summarizes the visible signs of bone regeneration at the defect-site.

Rabbit	Day 0	4th Week	8th Week	12th Week
1st	No distinct bonding observed.	Bone-bonding visible	Visible formation of bridging mass	No medullary cavity within the new bone mass.
2nd	Scaffold was less opaque.	Visible bone-bonding around the defect site.	Visible formation of bridging mass	No medullary cavity within the new bone mass.
3rd	No distinct bonding observed.	Poor bone-bonding	No indication of calcification	Bridging between the ends was observed at the defect site.
4th	Died post-operative Day 3			
5th	No distinct bonding observed.	Visible bone-bonding around the defect site.	Increase in radio-opacity.	Bridging between the ends was observed at the defect site.
6th Control	No distinct bonding observed.	No distinct observation noted.	No change in radio-opacity.	Bridging was absent at the defect site.

Table 4.13 List of signs and symptoms of the bone defect healing with the gain in recovery period in the experiment and control groups.

Extended osteoid areas and rTCGH entrapment by the new bone trabeculae were reflected as early as the 3rd week indictating the osteoconductivity. But rTCGH were degraded into lumps at 12th week post implantation. Absence of fibrous tissue demonstrates the osteointegration. Whereas, the control defect-site show no sign of bone remodelling till the12th week and remained empty.

Therefore, the 12 weeks' time point in *in vivo* study may not be sufficient to support complete ossification of the rTCGH scaffold. Indeed, the host cells surrounding the defect-site have been shown to invade the implant for mineralization of the scaffolds. Further reproducible *in vivo* studies involving large batch of animals are required to determine the ossification occurring in the scaffold implanted in the defect present at the load-bearing site in the long term [252].

In the orthotopic environment the mechanical cues (e.g. the hydrostatic pressure and dynamic compression) have shown to play key role in regulating MSCs phenotype and ECM production. The intrinsic behaviour of the ECM may also play drive the MSCs to osteoblast differentiation pathway.

4.4.3 Histological Examination

During the study, autopsy was performed by harvesting the treated rabbit bone specimens at 4, 8 and 12 weeks using succinyl chloride and sodium pentobarbital. The forearm was transferred to 4% formalin after it was dissected to remove the skin fascia and the muscle tissue. The '**critical-size defect'** in the five rabbits implanted with rTCGH, led to the formation of new bone. The bone-bonding led to ossification at the scaffold periphery in contact with the bone as observed from radio-opacity. The ossification extended to bridge the defect gap by 8th week. After about the 12th week, no medullary cavity was found, yet girth of the bridged mass was same as the bone filler.